

# Crosstalk between lymphoid and myeloid cells orchestrates glioblastoma immunity through Interleukin 10 signaling

**Vidhya Ravi**

Microenvironment and Immunology Research Laboratory, Medical Center, University of Freiburg, Germany <https://orcid.org/0000-0003-0062-2099>

**Nicolas Neidert**

Department of Neurosurgery, Medical Center, University of Freiburg, Germany

**Paulina Will**

Microenvironment and Immunology Research Laboratory, Medical Center, University of Freiburg, Germany

**Kevin Joseph**

Microenvironment and Immunology Research Laboratory, Medical Center, University of Freiburg, Germany

**Julian Maier**

Microenvironment and Immunology Research Laboratory, Medical Center, University of Freiburg, Germany

**Jan Kückelhaus**

Microenvironment and Immunology Research Laboratory, Medical Center, University of Freiburg, Germany

**Lea Vollmer**

Microenvironment and Immunology Research Laboratory, Medical Center, University of Freiburg, Germany

**Jonathan Goeldner**

Microenvironment and Immunology Research Laboratory, Medical Center, University of Freiburg, Germany

**Simon Behringer**

Department of Neurosurgery

**Florian Scherer**

Department of Medicine I, Medical Center – University of Freiburg, Faculty of Medicine, University of Freiburg, Germany

**Melanie Boerries**

Faculty of Medicine, Freiburg University, Germany

**Marie Follo**

University Medical Center

**Tobias Weiss**

University Hospital of Zurich

**Daniel Delev**

Department of Neurosurgery, RWTH University of Aachen, Aachen, Germany

**Julius Kernbach**

Department of Neurosurgery, RWTH University of Aachen, Aachen, Germany

**Pamela Franco**

Department of Neurosurgery

**Nils Schallner**

Faculty of Medicine, Freiburg University, Germany

**Christine Dierks**

Faculty of Medicine, Freiburg University, Germany

**Maria Stella Carro**

University Medical Center Freiburg <https://orcid.org/0000-0002-8570-7691>

**Ulrich Hofmann**

Department of Neurosurgery, Medical Center, University of Freiburg, Germany

**Christian Fung**

Department of Neurosurgery, Medical Center, University of Freiburg, Germany

**Roman Sankowski**

University of Freiburg <https://orcid.org/0000-0001-9215-8021>

**Marco Prinz**

University of Freiburg <https://orcid.org/0000-0002-0349-1955>

**Jürgen Beck**

University Medical Center Freiburg

**Oliver Schnell**

University Medical Center Freiburg

**Dieter Heiland** (✉ [Dieter.henrik.heiland@uniklinik-freiburg.de](mailto:Dieter.henrik.heiland@uniklinik-freiburg.de))

Medical Center, University of Freiburg <https://orcid.org/0000-0002-9258-3033>

---

**Article**

**Keywords:** cancer immunotherapy, Glioblastoma (GBM), T-cells, JAK/STAT inhibition

**Posted Date:** February 17th, 2021

**DOI:** <https://doi.org/10.21203/rs.3.rs-244157/v1>

**License:**   This work is licensed under a Creative Commons Attribution 4.0 International License.

[Read Full License](#)

---

**Version of Record:** A version of this preprint was published at Nature Communications on February 17th, 2022. See the published version at <https://doi.org/10.1038/s41467-022-28523-1>.

---

1 **Crosstalk between lymphoid and myeloid cells orchestrates glioblastoma**  
2 **immunity through Interleukin 10 signaling**

---

3  
4 **Vidhya M. Ravi**<sup>1,2,3,4,#</sup>, **Nicolas Neidert**<sup>1,2,3,#</sup>, **Paulina Will**<sup>1,2,3,#</sup>, Kevin Joseph<sup>1,2,3</sup>, Julian P. Maier<sup>1,2,3</sup>,  
5 Jan Kückelhaus<sup>1,2,3</sup>, Lea Vollmer<sup>1,2,3</sup>, Jonathan M Goeldner<sup>1,2,3</sup>, Simon P. Behringer<sup>1,2,3</sup>, Florian  
6 Scherer<sup>3,5</sup>, Melanie Boerries<sup>3,6,7,8</sup>, Marie Follo<sup>3,5</sup>, Tobias Weiss<sup>9</sup>, Daniel Delev<sup>10,11</sup>, Julius Kernbach<sup>10,11</sup>,  
7 Pamela Franco<sup>3,4</sup>, Nils Schallner<sup>3,12</sup>, Christine Dierks<sup>3,5</sup>, Maria Stella Carro<sup>2,3</sup>, Ulrich G. Hofmann<sup>3,4</sup>,  
8 Christian Fung<sup>2,3</sup>, Roman Sankowski<sup>3,13</sup>, Marco Prinz<sup>3,13,14,15</sup>, Jürgen Beck<sup>2,3,15</sup>, **Oliver Schnell**<sup>2,3,16,†</sup>,  
9 **Dieter Henrik Heiland**<sup>1,2,3 †</sup>

10  
11 <sup>1</sup>*Microenvironment and Immunology Research Laboratory, Medical Center, University of Freiburg,*  
12 *Germany*

13 <sup>2</sup>*Department of Neurosurgery, Medical Center, University of Freiburg, Germany*

14 <sup>3</sup>*Faculty of Medicine, Freiburg University, Germany*

15 <sup>4</sup>*Neuroelectronic Systems, Medical Center, University of Freiburg, Germany*

16 <sup>5</sup>*Department of Medicine I, Medical Center – University of Freiburg, Faculty of Medicine,*  
17 *University of Freiburg, Germany.*

18 <sup>6</sup>*Institute of Medical Bioinformatics and Systems Medicine, Medical Center-University of Freiburg,*  
19 *79110 Freiburg, Germany.*

20 <sup>7</sup>*Comprehensive Cancer Center Freiburg (CCCF), Faculty of Medicine and Medical Center - University*  
21 *of Freiburg, 79106 Freiburg, Germany.*

22 <sup>8</sup>*German Cancer Consortium (DKTK), partner site Freiburg.*

23 <sup>9</sup>*Department of Neurology and Brain Tumor Center, University Hospital Zurich and University of*  
24 *Zurich, Switzerland*

25 <sup>10</sup>*Department of Neurosurgery, RWTH University of Aachen, Aachen, Germany*

26 <sup>11</sup> *Neurosurgical Artificial Intelligence Laboratory Aachen (NAILA), Department of Neurosurgery,*  
27 *RWTH University of Aachen, Aachen, Germany*

28 <sup>12</sup>*Department of Anesthesiology and Critical Care Medicine, Medical Center-University of Freiburg,*  
29 *79106 Freiburg, Germany*

30 <sup>13</sup>*Institute of Neuropathology, Medical Center - University of Freiburg,*

31 <sup>14</sup>*Signalling Research Centres BIOSs and CIBSS, University of Freiburg, Germany*

32 <sup>15</sup>*Center for NeuroModulation (NeuroModul), University of Freiburg, Freiburg, Germany*

33 <sup>16</sup>*Translational NeuroOncology Research Group, Medical Center, University of Freiburg, Germany*

34 **# Equal contributed first authorship**

35 **† Equal contributed last authorship**

36  
37 **DISCLOSURE OF CONFLICTS OF INTEREST:** No potential conflicts of interest were  
38 disclosed by the authors.

40 **Corresponding author:**  
41 Dieter Henrik Heiland  
42 Department of Neurosurgery  
43 Medical Center University of Freiburg  
44 Breisacher Straße 64  
45 79106 Freiburg  
46 -Germany-  
47 Tel: +49 (0) 761 270 50010  
48 Fax: +49 (0) 761 270 51020  
49 E-mail: [dieter.henrik.heiland@uniklinik-freiburg.de](mailto:dieter.henrik.heiland@uniklinik-freiburg.de)

50 **Abstract**

51 Despite recent advances in cancer immunotherapy, its efficacy in Glioblastoma (GBM)  
52 is limited due to poor understanding of molecular states and cellular plasticity of  
53 immune cells within the tumor microenvironment. Here, we combined spatial and  
54 single-cell transcriptomics of 47,284 immune cells, to map the potential cellular  
55 interactions leading to the immunosuppressive microenvironment and dysfunction of T  
56 cells. Computational approach identified a subset of IL10 releasing *HMOX1*<sup>+</sup> myeloid  
57 cells which activates transcriptional programs towards a dysfunctional state in T cells,  
58 and was found to be localized within mesenchymal dominated subregions of the tumor.  
59 These findings were further validated by a human *ex-vivo* neocortical GBM model  
60 (n=6) coupled with patient derived peripheral T-cells. Finally, the dysfunctional  
61 transformation of T cells was shown to be rescued by JAK/STAT inhibition in both our  
62 model and *in-vivo*. We strongly believe that our findings would be the stepping stone  
63 towards successful development of immunotherapeutic approaches in GBM.

64  
65  
66  
67  
68  
69  
70  
71  
72  
73  
74  
75  
76  
77  
78  
79  
80  
81  
82  
83

84

## 85 **Introduction**

86 Tumor infiltrating lymphocytes, along with resident and migrated myeloid cells, account  
87 for a significant part of the tumor microenvironment in glioblastoma<sup>1-3</sup>. Most recently,  
88 the characterization of the myeloid cell population using scRNA-sequencing revealed  
89 remarkable heterogeneity with regards to cellular diversity and plasticity within the  
90 myeloid compartment<sup>1,4</sup>. However, the diversity of lymphoid cell types within malignant  
91 brain tumors remains unexplored and needs to be illuminated. Insights into the  
92 heterogeneity of cell type composition and driver genes for lineage differentiation within  
93 lymphoid compartment will aid in providing successful approaches for immunotherapy  
94 in the future. In other cancer entities such as colorectal cancer<sup>5</sup>, liver cancer<sup>6</sup> or  
95 melanoma<sup>7</sup>, different T cell states have been investigated. Situations which involve  
96 prolonged immune activation and ambiguous stimulation, such as uncontrolled tumor  
97 growth or chronic infections, impede the ability of CD8<sup>+</sup> lymphocytes to secrete  
98 proinflammatory cytokines and maintain their cytotoxic profile<sup>7-9</sup>. This cellular state,  
99 named dysfunctional or "exhausted" CD8<sup>+</sup> lymphocytes, represents a paramount  
100 barrier to successful immune-vaccination or checkpoint therapy<sup>2,10,11</sup>. T cell exhaustion  
101 is partially orchestrated by regulation of inhibitory cell surface receptors (PD-1, CTLA-  
102 4, LAG-3, TIM-3 and others), in addition to anti-inflammatory cytokines such as IL-10  
103 and TGF- $\beta$ . Glioblastoma, a common and very aggressive primary brain tumor in  
104 adults, is archetypical for tumors with a strong immunosuppressive microenvironment<sup>12</sup>.  
105 Current, immunotherapeutic approaches such as PDL1/PD1 checkpoint blockade<sup>13</sup> or  
106 peptide vaccination<sup>14</sup>, led to remarkable responses in several cancers, has failed to  
107 demonstrate its effectivity in patients suffering from glioblastoma.

108 To address the sparse knowledge with respect to the lymphoid cell population in  
109 glioblastoma, we performed deep transcriptional profiling by means of scRNA-  
110 sequencing, and mapped potential cellular interactions and cytokine responses that  
111 could lead to the dysfunctional and exhausted phenotype of T cells. Pseudotime  
112 analysis revealed an increased response to Interleukin 10 (IL10) during the  
113 transformation of T cells from the effector state to the dysfunctional state. To  
114 computationally explore "connected" cells driving this transformation, we introduced a  
115 novel approach termed "*nearest functionally connected neighbor (NFCN)*", which  
116 identified a subset of myeloid cells marked by *CD163<sup>+</sup>* and *HMOX1<sup>+</sup>* expression.  
117 Furthermore, we performed spatially resolved transcriptomics, which confirmed the

118 spatial overlap of exhausted T cells with *HMOX1*<sup>+</sup> myeloid cells, within regions of the  
119 tumor enriched with mesenchymal transcriptional signatures. Finally, using human  
120 neocortical GBM model (coupled with patient derived T cells) and myeloid cell  
121 depletion, we conclusively validated that myeloid cells are key drivers for  
122 immunosuppressive microenvironment in the glioblastoma. The dysfunctional  
123 transformation of T cells were found to be rescued by the JAK-STAT inhibition due to  
124 the reduction in IL10 release, as shown before <sup>15</sup>, in our ex-vivo model. Based on these  
125 results, we treated a single patient having recurrent glioblastoma in a neoadjuvant  
126 setting with JAK-STAT inhibitor (Ruxolitinib) and partially rescued the  
127 immunosuppressive environment.

128  
129  
130  
131  
132  
133  
134  
135  
136  
137  
138  
139  
140  
141  
142  
143  
144  
145  
146  
147  
148  
149  
150  
151



152 **Results:**

153 **Single cell Analysis of the Immune Cell Compartment in Glioblastoma**

154 In order to interrogate the diversity of the immune microenvironment in glioblastoma,  
155 we performed droplet based 10X single cell sequencing of tissue samples from 8  
156 patients, diagnosed with Glioblastoma. Lymphoid and myeloid populations  
157 (CD45<sup>+</sup>/CD3<sup>+</sup>) were sorted from neoplastic tissue specimens (**Figure 1a and**  
158 **Supplementary Figure 1a**). The scRNA-seq data consisted of 47,284 cells, with a  
159 median number of 2,301 unique molecular identifiers (UMIs) and approximately 1023  
160 uniquely expressed genes per cell. We corrected the data for mitochondrial genes,  
161 regressed out cell cycle effects and removed batch effects due to technical artifacts.  
162 We then decomposed the eigenvalue frequencies of the first 100 principal components  
163 and determined the number of non-trivial components by comparing them to  
164 randomized expression values, resulting in 41 meaningful components. Shared  
165 nearest neighbor (SNN) graph clustering resulted in 21 clusters (C0-C20) containing  
166 uniquely expressed genes. The major observed cell type when using the semi-  
167 supervised subtyping algorithm of scRNA-seq (SCINA-Model)<sup>16</sup> and SingleR<sup>17</sup> are:  
168 microglia cells (*TMEM119*, *CX3CR1* and *P2RY12*) and macrophages (*AIF1*, *CD68*,  
169 *CD163* and low expression of *TMEM119*, *CX3CR1*), followed by CD8<sup>+</sup> T cells (*CD8A*,  
170 *CD3D*), natural killer cells (*KLRD1*, *GZMH*, *GZMA*, *NKG7* and *CD52*), CD4<sup>+</sup> T cells  
171 (*BCL6*, *CD3D*, *CD4*, *CD84* and *IL6R*), T-memory cells (*TRBC2*, *LCK*, *L7R* and *SELL*),  
172 granulocytes (*LYZ*), a minor number of oligodendrocytes and oligodendrocyte-  
173 progenitor cell (OPC's) (*OLIG1*, *MBP*, *PDGFA*), and endothelial cells (*CD34*, *PCAM1*,  
174 *VEGFA*) **Figure 1b, Supplementary Figure 1b-f**. To identify malignant cells, we  
175 inferred large scale copy number variations (CNVs) from scRNA-seq profiles by  
176 averaging expression over stretches of 100 genes on their respective chromosomes<sup>18</sup>.  
177 With this approach, we confirmed that there was minimal contamination by tumor cells  
178 (clustered as OPC cells), based on their typical chromosomal alterations (gain in  
179 chromosome 7 and loss in chromosome 10), **Supplementary Figure 2a**.

180

181 **Diversity of T cells in the Glioblastoma Microenvironment**

182 To investigate the diversity of the T cells present in the microenvironment, we  
183 examined them by two different but complementary methods. Firstly, T cells were  
184 isolated *in-silico* by means of clustering (as shown above), based on previously  
185 published marker gene expression profiles (CD3<sup>+</sup>, CD4<sup>+</sup>/CD8<sup>+</sup>). Secondly, they were

186 isolated using the SCINA model, which resulted in a total of 7,547 cells  
187 **Supplementary Figure 1g**. Focusing on the different regulatory states of these cells,  
188 we identified 13 subclusters using SNN-clustering which were then re-embedded into  
189 a dynamic model using RNA-velocity, closely reflecting different activation states,  
190 **Supplementary Figure 1h and Figure 1c**. Reconstruction of lineage differentiation  
191 trajectories by means of both pseudotime and latent time provided insights into the  
192 transformation of the cells over time<sup>19</sup>, **Figure 1c**. Based on common marker  
193 signatures, we defined activated T cells by expressing *GZMA*, *CCL5* and *CCL4*, *IL7RI*  
194 and other markers (**Supplementary Figure 1i and 2b**) as well as increased  
195 proliferation (G2M-score, **Figure 1d**) (C1,C10), and naive T cells by the expression of  
196 *SELL*, *TCF7* and *CCR7* (C0), **Figure 1c and Supplementary Figure 1h**. We further  
197 identified T cell subgroups marked by hypoxia and heat-shock signaling (*HSPA8*, C2,  
198 C5,C6) and by a subgroup which showed mixed expression of  
199 activation/dysfunctional/exhaustion markers (*HAVCR2*, *GNLY*) and strong enrichment  
200 IL-10 signaling, **Figure 1d**. We estimated the G2M-score and identified a lower  
201 frequency of cell cycle in the differentiated/late states of T cells with the exception of  
202 the IFN-gamma subtype, **Figure 1d**. Additional marker plots are given in the  
203 **Supplementary Figure 2b**. Regulatory CD4+ T cells (*FOXP3*, *IL2RA* and *CTLA4*)  
204 represents a minor population in the glioblastoma microenvironment, **Figure 1c** and  
205 **Supplementary Figure 1i-j**.

### 206 **Dysfunctional State of T cells is Driven by IL-10 Signaling**

207 To gain insights into the regulatory mechanism of immune cells, we reconstructed fate  
208 decisions made during T cell exhaustion using pseudotime trajectories along the  
209 estimated velocity streams, **Figure 1e**. Using RNA-velocity, we estimated cells with  
210 high probability of initial and terminal states which resulted in 3 major branches with  
211 unique cell fate drivers, **Figure 1e**. In order to determine the dynamic adaptation  
212 across all branches (Velo trajectory 1-3), we computed pseudotime vectors using  
213 various models. Only two trajectories confirmed the predicted ascending pseudotime  
214 inference across multiple models (*HAVCR2*(+)-T cells and hypoxia-induced T cells),  
215 **Figure 1f**. We assume that terminal states without significant pseudotime connection  
216 do not inevitably arise from the determined initial state, which suggests that the lineage  
217 of IFN-gamma driven T cells coexists and most likely originated from an earlier lineage  
218 branch **Figure 1g**.

219 Along our trajectory from effector to HAVCR2(+)T cells, we showed a latent time-  
220 dependent increase of the response to anti-inflammatory signaling such as IL-10 and  
221 TGF-beta signaling **Figure 1h**. Next, we mapped the gene expression of defined  
222 exhausted and effector signatures along our differentiation trajectory, revealing an  
223 enrichment of exhausted genes within the destination cluster. Thus, our data suggests  
224 that this response to IL-10 contributes to the dysfunctional state of T cells and affects  
225 fate decisions **Figure 1i**. To gain further insights into accurate downstream signaling  
226 of IL-10, IFN-gamma, and IL2, we created a library of the 50 most highly up- and  
227 downregulated genes, **Supplementary Figure 3a-b**. We then extracted signatures  
228 observed within the different T cell clusters and compared them with stimulated T cells.  
229 As expected, genes upregulated by IL2 stimulation were significantly enriched in  
230 cluster 1, while signature genes from IFN-gamma stimulation was enriched in cluster  
231 12. Signature genes from IL-10 stimulation showed a significant enrichment in the  
232 dysfunctional cluster (Cluster 9), **Supplementary Figure 3c**. Furthermore, we mapped  
233 our signatures along our defined velocity trajectory 1 which confirmed our predicted  
234 pathway inference, **Figure 1j-k and Supplementary Figure 3d**.

235

### 236 **T cell Activation and Exhaustion Reveals Spatial Heterogeneity and Association** 237 **with Glioblastoma Subtypes**

238 Glioblastomas present a high degree of heterogeneity due to regional metabolic  
239 differences and varying composition of the tumor microenvironment<sup>20</sup>. To decipher the  
240 spatial distribution of above illustrated T cell clusters and its colocalization to defined  
241 tumor states, we performed spatial transcriptomic RNA sequencing (stRNA-seq) of 3  
242 primary IDH1/2 wildtype glioblastoma, containing a total number of 2,352 spots, **Figure**  
243 **2a**. We observed a median of 8 cells per spot (range: 4 to 22 cells per spot), which  
244 allows the spatial mapping of gene expression, but not at single cell resolution.  
245 However, when we compared our dataset to the latest classification of glioblastoma<sup>20</sup>,  
246 consistent results were obtained in accordance with the diversity of subtype  
247 expression, **Figure 2b**. In particular, Neftel and colleagues raised evidence that the  
248 mesenchymal gene expression is more likely associated with immune response and  
249 cellular interaction to myeloid cells<sup>20</sup>. In order to investigate the spatial distribution of  
250 the mesenchymal subgroup, we performed gene set enrichment analysis at spatial  
251 resolution which revealed spot-wise enrichments within all samples, **Figure 2c-d**. In a  
252 next step, we used a seeded non-negative matrix factorization (NMF) regression<sup>21</sup> to

253 estimate the probability of individual T cell clusters at spatial resolution, **Figure 2e**. We  
254 computed the spatial overlap of T cell clusters and glioblastoma states, using a  
255 Bayesian approach, which revealed a high estimated correlation of the mesenchymal  
256 and T cell cluster 3 (T HAVCR2), cluster 5-7 (T Hypoxia), **Figure 2f**. Further analysis  
257 confirmed the strong overlap of dysfunctional/exhausted marker (LAG3 and HAVCR2)  
258 exclusively with the mesenchymal gene expression signature, **Figure 2g**, suggesting  
259 that our data support the findings from Neftel and colleagues.

260

### 261 **A Subset of Microglia and Macrophages Drive IL-10 Stimulation**

262 In our recent investigation<sup>15</sup>, the crosstalk between microglia cells and reactive  
263 astrocytes in the tumor microenvironment was found to be responsible for upregulating  
264 IL10 release. This is mediated by microglia/macrophages stimulated with IFN gamma,  
265 leading to JAK/STAT activation in tumor-associated astrocytes. In this study we  
266 introduce the “nearest functionally connected neighbor” algorithm (NFCN), an in-silico  
267 model to identify the most likely related cell pairs through divergent down- and up-  
268 stream signal activity, **Figure 3a**. With our model, we assume that cellular interaction  
269 with distinct mutual activation implies two fundamental prerequisites. On the one hand,  
270 the ligand needs to be expressed and released, or otherwise exposed on the cell  
271 surface. To avoid the chances of randomly elevated expression or technical artifacts,  
272 we also looked at the simultaneous occurrence of ligand induction (upstream pathway  
273 signaling). On the other hand, the receptor needs to be expressed and, additionally,  
274 downstream signaling has to be activated as well. This allows us to predict the  
275 functional status of the receiver cell (Explanation of the model can be found in the  
276 Methods section, with an overview in **Supplementary Figure 4**). We used our *in-silico*  
277 model to screen for potential cells responsible for IL-10 activation of T cells. The  
278 algorithm identified pairs of lymphoid (T cell clusters) and myeloid cells (macrophages  
279 and microglia cluster) and estimated the likelihood of mutual activation **Figure 3b,c**.  
280 By extraction of the nearest connected cells (top 1% ranked cells), we identified a  
281 subset of myeloid cells characterized by remarkably high *IL10* expression. Most of the  
282 receiver cells in the connected cells (top 1% ranked cells) originated from the T cell  
283 cluster **Figure 3d**. Our predicted IL10 interactions were also supported by another  
284 computational approach (**Supplementary Figure 5**). In order to validate our  
285 computational model, we used SPOTlight<sup>21</sup>, an algorithm to predict the spatial position  
286 of cells from scRNA-seq data, and were able to confirm a significant overlap. In order  
287 to explore the difference between connected and non-connected cells, we extracted

288 both connected and non-connected cells, defined by the highest and lowest  
289 interaction-scores (quantile 97.5%) Using differential gene expression analysis, we  
290 observed multiple genes which confirmed the non-inflammatory polarization status of  
291 highly connected cells.

292 These findings are not surprising, since one of the essential markers of non-  
293 inflammatory myeloid cells is *IL10*, **Figure 3e**. We showed that the subset of most  
294 highly connected cells were marked by *CD163* and heme oxygenase 1 (*HMOX1*)  
295 expression. In a multilayer representation, we illustrated the estimated cellular  
296 connections with respect to their most likely spatial coordinates, **Figure 3f**. *HMOX1* is  
297 activated during inflammation and oxidative injuries and is regulated through the  
298 Nrf2/Bach1-axis, as well as through the IL10/HMOX1-axis. This gene is also well  
299 known to be upregulated in the alternative activated macrophage subtype<sup>22</sup>. Another  
300 immunosuppressive signaling marker closely related to the alternative activation of  
301 macrophages/microglia is the release of TGF- $\beta$ <sup>23</sup>, which was also found to be up-  
302 regulated in highly connected cells, **Figure 3g**. Consistent with our findings, most  
303 downstream signals of the IL10/HMOX1-axis such as STAT3 and p38 MAPK were  
304 found to be upregulated in a gene set enrichment analysis, **Figure 3d,h**. In a recent  
305 investigation, the role of doublets in the detection of cell-cell interactions was  
306 described<sup>24</sup>. In our dataset the score of potential cell-cell connections was similar to  
307 HMOX1 marked macrophages, within the doublet dominated cluster. We computed  
308 the marker genes of our predicted connected myeloid and lymphoid genes and found  
309 each of the marker sets to be highly expressed in the doublet cluster, which further  
310 validated the results from our computational model, **Figure 3i**.

311

### 312 **Loss of Myeloid Cells Increases Antitumor Immunity**

313 To validate our computational findings, we made use of the recently described human  
314 neocortical GBM model, where the cellular architecture of the CNS is well preserved  
315 <sup>15,25</sup>. We cultured non-infiltrated neocortical slices (defined in a recent report<sup>15,25</sup>)  
316 coupled with autografted T cells along with myeloid cell depletion, to understand the  
317 communication between myeloid cells in the tumor microenvironment along with  
318 lymphoid cells. Three days after chemical depletion of the myeloid cells, we injected a  
319 primary cell line (BTSC#233, GFP-tagged, previously characterized by RNA-seq  
320 profiling as mesenchymal)<sup>26</sup>. After 4 days of culture, peripheral T cells (same donors),  
321 tagged using CellTrace™ Far Red (CTFR) were additionally inoculated and the  
322 sections were further cultured for another 48h, **Figure 4a**. Immunostainings showed

323 that myeloid cell depletion reduces the number of IBA1<sup>+</sup>HMOX1<sup>+</sup> cells, **Figure 4b**.  
324 Using an enzyme-linked immunosorbent assay (ELISA) we found a significant  
325 reduction in IL10 when the myeloid cells were depleted, regardless of the presence of  
326 tumor cells. The strongest difference in IL10 release was observed in myeloid cell  
327 depleted sections in the presence of tumor cells, **Figure 4c**. Furthermore, we stained  
328 for Granzyme B (GZMB<sup>+</sup>) T cells and quantified IL2 release to examine the amount of  
329 effector T cells in both the depleted and non-depleted sections. We found an increased  
330 number of GZMB<sup>+</sup> T cells in sections with myeloid cell depletion, **Figure 4d**, along with  
331 a significant increase in IL2 and no differences in IFN gamma release were observed,  
332 **Figure 4e-f**. We also stained for the exhaustion marker TIM3 (Gen: *HAVCR2*), which  
333 was found to be enriched in T cells in the presence of myeloid cell **Figure 4g**,  
334 suggesting that myeloid derived IL10 release (by HMOX1<sup>+</sup> cells) leads to T cell  
335 exhaustion, which is in agreement with the computational model. In order to prove that  
336 the IL10 signaling is responsible for the induction of the expression of exhausted T cell  
337 markers, we preincubated T cells using an IL10 neutralizing inhibitory antibody **Figure**  
338 **4h**. This resulted in a strong increase of GZMB<sup>+</sup> T cells, followed by a significant  
339 increase of IL2, suggesting that IL10 inhibition drives T cell activity, **Figure 4i-j**. From  
340 our recent study, we found that a JAK/STAT inhibition causing a significant reduction  
341 of IL10 within the tumor microenvironment<sup>15</sup>. Based on this investigation, we pre-  
342 treated tissue sections with Ruxolitinib, an FDA-approved JAK-inhibitor, before  
343 inoculating the sections with patient-derived T cells. We were able to confirm that JAK  
344 inhibition caused a significant decrease of IL10 and increased levels of the  
345 inflammatory marker IL2, **Figure 4k-l**.

346 Based on our above findings, we treated a first patient with a recurrent glioblastoma in  
347 a neoadjuvant setting with Ruxolitinib for 4 weeks. After resection, we sorted CD45<sup>+</sup>  
348 cells and performed scRNA-sequencing **Figure 4m**. Immunostainings of the tumor  
349 revealed a relative increase of CD8<sup>+</sup> and CD4<sup>+</sup> T cells whereas CD68<sup>+</sup> myeloid cells  
350 remained stable, **Figure 4n-o**. scRNA sequencing revealed a large number of T cells,  
351 most of which express markers for T cell activation and a few cells showing a naive  
352 signature, **Figure 4p**. When compared with T cells from our initial dataset, an  
353 enrichment of the T cells from the JAK treated patient was seen within cluster 1  
354 (activated T cells) and cluster 12 (B cells), suggesting that JAK-inhibition could be a  
355 potential treatment option to boost T cell activation by reducing immunosuppressive  
356 programs in both myeloid and glial cells, **Figure 4q-r**.

357

358 **Discussion:**

359 Although single-cell RNA-sequencing accurately maps the cellular architecture and  
360 reflects the diversity of cellular states<sup>18,20,27,28</sup>, there is a lack of spatial information.  
361 Here, we combine single cell RNA sequencing of the immune compartment along with  
362 spatial transcriptomic RNA-sequencing (stRNA-seq) to gain better insights into the  
363 complex crosstalk, cellular states and cellular plasticity leading to the  
364 immunosuppressive environment found in glioblastoma (GBM).

365 Recent studies have reported different subtypes of microglia and macrophages  
366 occupying glial tumors<sup>1,4,20,27,28</sup>. However, detailed information about lymphoid  
367 infiltration cells is lacking. There is intense interest in T cells and their varied states  
368 due to their importance in the development of targeted therapies and to further the  
369 understanding of the immunosuppressive environment of glioblastoma. T cell states,  
370 particularly in disease, are somehow difficult to accurately classify, leading to  
371 numerous definitions and markers in recent years<sup>2,7,29-31</sup>. Some authors use the terms  
372 "dysfunctional" and "exhausted" synonymously<sup>32</sup>, whereas others differentiate  
373 between the dysfunctional and the exhausted states of T cells<sup>29,31</sup>. In this study we use  
374 the definition of cellular states proposed by Singer et al., 2016<sup>8</sup>. On the basis of these  
375 gene sets, our data showed that only cells which remained activated along the  
376 pseudotime-trajectory were able to enter a state of dysfunction, and later exhaustion.  
377 The dysfunction appears to be a transient state, associated with increased  
378 proliferation, despite immunosuppressive stimulation from the tumor environment. This  
379 imbalance between pro- and anti-inflammatory signaling, dominated by IL10 secretion,  
380 leads to final exhaustion of the T cells, which is in agreement with the current  
381 literature<sup>2,33</sup>. In order to find a consensus with regard to marker genes we further  
382 validated our findings on a set of exhausted marker genes recently published in an  
383 overview study<sup>34</sup>. We and others have shown that the GBM microenvironment aids in  
384 the evolution of immune suppression. In this process, astrocytes and myeloid cells,  
385 both driven by STAT-3 signaling, orchestrate the immunosuppressive  
386 environment<sup>4,15,35,36</sup>. Based on the knowledge that IL10 interaction plays a crucial role  
387 in the shift from activated to exhausted T cells, we built an *in-silico* model that identified  
388 potential connected cells driving T cell exhaustion.

389 Using this model, we identified a subset of myeloid cells marked by high expression of  
390 *HMOX1*<sup>+</sup>, a gene which is induced by oxidative stress and metabolic imbalance<sup>37,38</sup>.  
391 *HMOX1* is linked to the STAT-3 pathway and induces IL10 production via MAPK

392 activation, and all of these markers were also found to be upregulated in our connected  
393 cells, as reported above. Furthermore, we used spatial transcriptomics to confirm the  
394 spatial overlap of cells that we identified are highly connected. We were able to show  
395 that the *HMOX1*<sup>+</sup>-myeloid cells were spatially correlated with exhaustion and the  
396 mesenchymal state of glioblastoma. These findings are in accord with published  
397 reports, revealing that the mesenchymal cells are the component of GBM responsible  
398 for the immune crosstalk<sup>20</sup>. *HMOX1* expression in GBM and IDH-WT astrocytoma was  
399 found to be increased in recurrent GBM and negatively associated with overall survival,  
400 **Supplementary Figure 6a,b**. In addition, we made use of a human neocortical GBM  
401 model coupled with patient derived T cells with/without myeloid cell depletion. This  
402 model helped us to simulate the function of the myeloid cells with regard to IL10 release  
403 and T cell stimulation. Fitting with our computational model, we confirmed that  
404 *HMOX1*<sup>+</sup> myeloid cells cause a reduction of effector T cells, with a respective reduction  
405 in IL2 release and increased expression of our identified exhaustion marker TIM3.  
406 Following our recent investigations in which we demonstrated that JAK-inhibition is  
407 able to reduce the level of IL10 in human brain tumors<sup>15</sup>, we demonstrated that in a  
408 single patient that inhibition of the JAK-STAT axis was able to partially rescue the  
409 immunosuppressive environment. The treated subject is still alive but showed  
410 permanent disruption of the blood-brain barrier with repetitive increase of contrast  
411 enhancing lesions. Each radiologically confirmed progress was sampled without  
412 evidence of a tumor recurrence, suggesting that manipulation of the glia/myeloid  
413 environment simultaneously caused exaggerated inflammation and pseudo  
414 progression. Our single-cell RNA-seq confirmed a pronounced enrichment of activated  
415 T cells, while the number of myeloid cells remained relatively stable. In this sample,  
416 we also detected the strongest contamination with glial cells. We assumed that  
417 potential doublets or strong cell-cell connections led to glial cells being detected as  
418 CD45<sup>+</sup>, resulting in a false positive sorting.

419 In conclusion, this work provides the first knowledge regarding lymphocyte population  
420 in the glioblastoma microenvironment where we showed that the functional interaction  
421 between myeloid and lymphoid cells, leads to a dysfunctional state of T cells. Using  
422 human neocortical GBM model and single patient subject we showed that the IL-10  
423 driven T cell exhaustion can be rescued by JAK/STAT inhibition. Thus, the results from  
424 this work can be the steppingstone towards successful immunotherapeutic  
425 approaches for GBM.



426 **Methods:**

427 **Ethical Approval**

428 The local ethics committee of the University of Freiburg approved the data evaluation,  
429 imaging procedures and experimental design (protocol 100020/09 and  
430 472/15\_160880). The methods were carried out in accordance with the approved  
431 guidelines, with written informed consent obtained from all subjects. The studies were  
432 approved by an institutional review board. Further information and requests for  
433 resources, raw data and reagents should be directed and will be fulfilled by the Contact:  
434 D. H. Heiland, dieter.henrik.heiland@uniklinik-freiburg.de. A complete table of all  
435 materials used is given in the supplementary information.

436

437 **T cell isolation and stimulation**

438 Blood was drawn from a healthy human individual into an EDTA  
439 (ethylenediaminetetraacetic acid) cannula. T cells were extracted in a negative  
440 selection manner using a MACSxpress® Whole Blood Pan T Cell Isolation Kit (Miltenyi  
441 Biotech). T cells were then transferred in Advanced RPMI 1640 Medium  
442 (ThermoFisher Scientific, Pinneberg, Germany) and split for cytokine treatment: Three  
443 technical replicates were used for each T cell-treatment condition. Interleukin 2 (IL-2,  
444 Abcam, Cambridge, UK) was used at a final concentration of 1 ng/ml, Interleukin 10  
445 (IL-10, Abcam) at 5 ng/ml, Interferon gamma (IFN- $\gamma$ , Abcam) at 1 ng/ml and  
446 Osteopontin (SPP-1, Abcam) at 3  $\mu$ g/ml. Cytokine treatment was performed in  
447 Advanced RPMI 1640 Medium and T cells were incubated at 37°C and 5% CO<sub>2</sub> for  
448 24h.

449

450 **RNA sequencing of stimulated T Cells**

451 The purification of mRNA from total RNA samples was achieved using the Dynabeads  
452 mRNA Purification Kit (Thermo Fisher Scientific, Carlsbad, USA). The subsequent  
453 reverse transcription reaction was performed using SuperScript IV reverse  
454 transcriptase (Thermo Fisher Scientific, Carlsbad, USA). For preparation of RNA  
455 sequencing, the Low Input by PCR Barcoding Kit and the cDNA-PCR Sequencing Kit  
456 (Oxford Nanopore Technologies, Oxford, United Kingdom) were used as  
457 recommended by the manufacturer. RNA sequencing was performed using the  
458 MinION Sequencing Device, the SpotON Flow Cell and MinKNOW software (Oxford  
459 Nanopore Technologies, Oxford, United Kingdom) according to the manufacturer's

460 instructions. Samples were sequenced for 48h on two flow-cells. Basecalling was  
461 performed by Albacore implemented in the nanopore software. Only D<sup>2</sup>-Reads with a  
462 quality Score above 8 were used for further alignment.

463

### 464 **Sequence trimming and Alignment**

465 In the framework of this study, we developed an automated pipeline for nanopore  
466 cDNA-seq data, which is available at github  
467 (<https://github.com/heilandd/NanoPoreSeq>). First the pipeline set up a new class  
468 termed “Poreseq” by a distinct sample description file. The analysis starts by  
469 rearranging the reads from the *fastq* output from the nanopore sequencer containing  
470 all of the D<sup>2</sup>-Reads. All *fastq* files need to be combined into one file. Multiplexed  
471 samples were separated according to their barcode and trimmed by Porechop  
472 (<https://github.com/rrwick/Porechop>). Alignment was performed with minimap2  
473 (<https://github.com/lh3-/minimap2>) and processed with sam-tools.

474

### 475 **Posthoc Analysis of Bulk-RNA-seq**

476 A matrix of counted genes was further prepared by the RawToVis.R  
477 ([github.com/heilandd/VRSD\\_Lab\\_v1.5](https://github.com/heilandd/VRSD_Lab_v1.5)) script, containing normalization of Mapped  
478 reads by DESeq, batch effect removal (ComBat package) and fitting for differential  
479 gene expression. Gene set enrichment analysis was performed by transformation of  
480 the log<sub>2</sub> fold-change of DE into a ranked z-scored matrix, which was used as the input.  
481 The expression matrix was analysed with AutoPipe  
482 (<https://github.com/heilandd/AutoPipe>) by a supervised machine-learning algorithm  
483 and visualized with a heatmap. Full analysis was visualized with the Visualization of  
484 RNA-Seq Data (VRSD\_Lab software, [github.com/heilandd/VRSD\\_Lab\\_v1.5](https://github.com/heilandd/VRSD_Lab_v1.5)) as a  
485 dashboard app based on shiny R-software. We extracted the 50 top up/down regulated  
486 genes respectively of each stimulation with respect to control condition to construct a  
487 stimulation library.

488

### 489 **Single-Cell Suspension for scRNA-sequencing**

490 Tumor tissue was obtained from glioma surgery immediately after resection and was  
491 transported in phosphate-buffered saline (PBS) within approximately 5 minutes into  
492 our cell culture laboratory. Tumor tissue was processed under a laminar flow cabinet.  
493 Tissue was reduced to small pieces using two scalpels and the tissue was processed

494 with the Neural Tissue Dissociation Kit (T) using C-Tubes (Miltenyi Biotech, Bergisch-  
495 Gladbach, Germany) according to the manufacturer's instructions. The Debris  
496 Removal Kit from Miltenyi was used according to the manufacturer's instructions to  
497 remove remaining myelin and extracellular debris. In order to remove the remaining  
498 erythrocytes, we resuspended the pellet in 3,5 ml ACK lysis buffer (ThermoFisher  
499 Scientific, Pinneberg, Germany) and incubated the suspension for 5 minutes followed  
500 by a centrifugation step (350g, 10 min, RT). Cell quantification with a hemacytometer  
501 was performed after discarding the supernatant and resuspending the pellet in PBS.  
502 Cell suspensions were centrifuged again (350g, 10 min, RT) and resuspended in  
503 freezing medium containing 10% DMSO (Sigma-Aldrich, Schnellendorf, Germany) in  
504 FCS (PAN-Biotech, Aidenbach, Germany). Cell suspensions were immediately placed  
505 in a freezing box containing isopropanol and stored in a -80°C freezer for not more  
506 than 4 weeks.

507

#### 508 **Cell sorting by Magnetic Beads**

509 Four frozen single-cell suspensions, originating from one patient with an IDH-mutated  
510 glioma and three patients with an IDH-wildtype glioblastoma (GBM), were thawed and  
511 the dead cells magnetically labeled and eliminated using a Dead Cell Removal Kit  
512 (Miltenyi Biotech). The tumor immune environment in general and T cells in particular  
513 were positively selected by using CD3<sup>+</sup>-MACS (Miltenyi Biotech). Cells were stained  
514 with trypan blue, counted using a hemacytometer and prepared at a concentration  
515 of 700 cells/ $\mu$ L.

516

#### 517 **Droplet scRNA-sequencing**

518 At least 16000 cells per sample were loaded on the Chromium Controller (10x  
519 Genomics, Pleasanton, CA, USA) for one reaction of the Chromium Next GEM Single  
520 Cell 3' v3.1 protocol (10x Genomics), based on a droplet scRNA-sequencing approach.  
521 Library construction and sample indexing was performed according to the  
522 manufacturer's instructions. scRNA-libraries were sequenced on a NextSeq 500/550  
523 High Output Flow Cell v2.5 (150 Cycles) on an Illumina NextSeq 550 (Illumina, San  
524 Diego, CA, USA). The bcl2fastq function and the cell ranger (v3.0) was used for quality  
525 control.

526

527

## 528 **Postprocessing scRNA-sequencing**

529 We used cell ranger to detect low-quality read pairs of single-cell RNA sequencing  
530 (scRNA-seq) data. We filtered out reads which did not reach the following criteria: (1)  
531 bases with quality < 10, (2) no homopolymers (3) 'N' bases accounting for  $\geq 10\%$  of the  
532 read length. Filtered reads were mapped by STAR aligner and the resulting filtered  
533 count matrix further processed by Seurat v3.0 (R-package). We normalized gene  
534 expression values by dividing each estimated cell by the total number of transcripts  
535 and multiplied by 10,000, followed by natural-log transformation. Next, we removed  
536 batch effects and scaled data by a regression model including sample batch and  
537 percentage of ribosomal and mitochondrial gene expression. For further analysis we  
538 used the 2000 most variable expressed genes and decomposed eigenvalue  
539 frequencies of the first 100 principal components and determined the number of non-  
540 trivial components by comparison to randomized expression values. The obtained non-  
541 trivial components were used for SNN clustering followed by dimensional reduction  
542 using the UMAP algorithm. Differently expressed genes (DE) of each cluster were  
543 obtained using a hurdle model tailored to scRNA-seq data which is part of the MAST  
544 package. Cell types were identified by 3 different methods; Classical expression of  
545 signature markers of immune cells; SingleR an automated annotation tool for single-  
546 cell RNA sequencing data obtaining signatures from the Human Primary Cell Atlas,  
547 SCINA, a semi-supervised cell type identification tool using cell-type signatures as well  
548 as a Gene-Set Variation Analysis (GSVA). Results were combined and clusters were  
549 assigned to the cell type with the highest enrichment within all models. In order to  
550 individually analyze T cells, we used the assigned cluster and filter for the following  
551 criteria. For further analysis T cells were defined by:  $CD3^+CD8^+$  /  $CD4^+CD14^-LYZ^-$   
552  $GFAP^-CD163^-IBA^-$ .

553

## 554 **Spatial Transcriptomics**

555 The spatial transcriptomics experiments were done using the 10X Spatial  
556 transcriptomics kit (<https://spatialtranscriptomics.com/>). All the instructions for Tissue  
557 Optimization and Library preparation were followed according to the manufacturer's  
558 protocol. Here, we briefly describe the methods followed using the library preparation  
559 protocol.

560

561

562 **Tissue collection and RNA quality control:**

563 Tissue samples from three patients, diagnosed with WHO IV glioblastoma multiforme  
564 (GBM), were included in this study. Fresh tissue collected immediately post resection  
565 was quickly embedded in optimal cutting temperature compound (OCT, Sakura) and  
566 snap frozen in liquid N<sub>2</sub>. The embedded tissue was stored at -80°C until further  
567 processing. A total of 10 sections (10µm each) per sample were lysed using TriZOL  
568 (Invitrogen, 15596026) and used to determine RNA integrity. Total RNA was extracted  
569 using PicoPure RNA Isolation Kit (Thermo Fisher, KIT0204) according to the  
570 manufacturer's protocol. RIN values were determined using a 2100 Bioanalyzer (RNA  
571 6000 Pico Kit, Agilent) according to the manufacturer's protocol. It is recommended to  
572 only use samples with an RNA integrity value >7.

573

574 **Tissue staining and Imaging:**

575 Sections were mounted onto spatially barcoded glass slides with poly-T reverse  
576 transcription primers, with one section per array. These slides can be stored at -80°C  
577 until use. The slides were then warmed to 37°C, after which the sections were fixed for  
578 10 minutes using 4% formaldehyde solution (Carl Roth, P087.1), which was then  
579 washed off using PBS. The fixed sections were covered with propan-2-ol (VWR,  
580 20842312). Following evaporation for 40 seconds, sections were incubated in Mayer's  
581 Hematoxylin (VWR, 1092490500) for 7 min, bluing buffer (Dako, CS70230-2) for 90  
582 seconds and finally in Eosin Y (Sigma, E4382) for 1 min. The glass slides were then  
583 washed using RNase/DNase free water and incubated at 37°C for 5 min or until dry.  
584 Before imaging, the glass slides were mounted with 87% glycerol (AppliChem, A3739)  
585 and covered with coverslips (R. Langenbrinck, 01-2450/1). Brightfield imaging was  
586 performed at 10x magnification with a Zeiss Axio Imager 2 Microscope, and post-  
587 processing was performed using ImageJ software.

588 The coverslips and glycerol were removed by washing the glass slides in  
589 RNase/DNase free water until the coverslips came off, after which the slides were  
590 washed using 80% ethanol to remove any remaining glycerol.

591

592 **Permeabilization, cDNA synthesis and tissue removal:**

593 For each capture array, 70µL of pre-permeabilization buffer, containing 50U/µL  
594 Collagenase along with 0.1% Pepsin in HCl was added, followed by an incubation for  
595 20 minutes at 37°C. Each array well was then carefully washed using 100µL 0.1x SSC

596 buffer. 70 $\mu$ L of Pepsin was then added and incubated for 11 minutes at 37°C. Each  
597 well was washed as previously described and 75 $\mu$ L of cDNA synthesis master mix  
598 containing: 96 $\mu$ L of 5X First strand buffer, 24  $\mu$ L 0.1M DTT, 255.2 $\mu$ L of DNase/RNase  
599 free water, 4.8 $\mu$ L Actinomycin, 4.5 $\mu$ L of 20mg/mL BSA, 24 $\mu$ L of 10mM dNTP, 48 $\mu$ L of  
600 Superscript® and 24 $\mu$ L of RNaseOUT™ was added to each well and incubated for 20  
601 hours at 42°C without shaking. Cyanine 3-dCTP was used to aid in the determination  
602 of the footprint of the tissue section used.

603 Since glioblastoma tissue is a fatty tissue, degradation and tissue removal was carried  
604 out using Proteinase K treatment for which 420 $\mu$ L Proteinase K and PKD buffer (1:7),  
605 were added to each well and then incubated at 56°C for 1hr with intermittent agitation  
606 (15 seconds / 3 minutes). After incubation, the glass slides were washed three times  
607 with 100mL of 50°C SSC/SDS buffer with agitation for 10 minutes, 1 minute and finally  
608 for 1 minute at 300 rpm. The glass slides were then air-dried at room temperature.  
609 Tissue cleavage was carried out by the addition of 70 $\mu$ L of cleavage buffer (320 $\mu$ L  
610 RNase/DNase free water, 104 $\mu$ L Second strand buffer, 4.2 $\mu$ L of 10mM dNTP , 4.8 $\mu$ L  
611 of 20 mg/mL BSA and 48 $\mu$ L of USER™ Enzyme) to each well and incubation at 37°C  
612 for 2 hours with intermittent agitation.

613

#### 614 **Spot Hybridization:**

615 In order to determine the exact location and quality of each of the 1007 spots,  
616 fluorescent Cyanine-3 A is hybridized to the 5' ends of the surface probes. 75 $\mu$ L of the  
617 hybridization solution (20 $\mu$ L of 10 $\mu$ M Cynaine-3A probe and 20 $\mu$ L of 10 $\mu$ M Cyanine-3  
618 Frame probe in 960 $\mu$ L of 1X PBS) was added to each well and incubated for 10min at  
619 room temperature. The slides were then washed three times with 100ml of SSC/SDS  
620 buffer preheated to 50°C for 10min, 1min and 1min at room temperature with agitation.  
621 The slides were then air-dried and imaged after applying Slowfade® Gold Antifade  
622 medium and a coverslip.

623

#### 624 **Library Preparation:**

##### 625 **1. Second Strand Synthesis**

626 5 $\mu$ L second strand synthesis mix containing 20 $\mu$ L of 5X First Strand Buffer, 14 $\mu$ L of  
627 DNA polymerase I (10U/ $\mu$ L) and 3.5 $\mu$ L Ribonuclease H (2U/ $\mu$ L) were added to the  
628 cleaved sample and incubated at 16°C for 2 hours. Eppendorf tubes were placed on

629 ice and 5 $\mu$ L of T4 DNA polymerase (3U/ $\mu$ L) were added to each strand and incubated  
630 for 20 minutes at 16°C. 25 $\mu$ L of 80mM EDTA (mix 30 $\mu$ L of 500mM EDTA with 158 $\mu$ L  
631 DNase/RNase free water) was added to each sample and the samples were kept cool  
632 on ice.

## 633 **2. cDNA purification**

634 cDNA from the previous step was purified using Agencourt RNAClean XP beads and  
635 DynaMag<sup>TM</sup>- 2 magnetic rack, incubated at room temperature for 5 min. Further  
636 cleansing was performed by the addition of 80% Ethanol to the sample tubes, while  
637 the samples were still placed in the magnetic rack. Sample elution was then carried  
638 out using 13 $\mu$ L of NTP/water mix.

## 639 **3. *In Vitro* Transcription and Purification**

640 cDNA transcription to aRNA was carried out by adding 4 $\mu$ L of reaction mix containing:  
641 10x Reaction Buffer, T7 Enzyme mix and SUPERaseIn<sup>TM</sup> RNase Inhibitor (20 U/ $\mu$ L) to  
642 12 $\mu$ L of the eluted cDNA sample and incubated at 37°C, for 14 hours. The samples  
643 were purified using RNA clean XP beads according to the manufacturer's protocol and  
644 further eluted into 10 $\mu$ L DNase/RNase free water. The amount and average fragment  
645 length of amplified RNA was determined using the RNA 6000 Pico Kit (Agilent, 5067-  
646 1513) with a 2100 Bioanalyzer according to the manufacturer's protocol.

## 647 **4. Adapter Ligation**

648 Next, 2.5 $\mu$ L Ligation adapter (IDT) was added to the sample and was heated for 2 min  
649 at 70°C and then placed on ice. A total of 4.5 $\mu$ L ligation mix containing 11.3 $\mu$ L of 10X  
650 T4 RNA Ligase, T4 RNA truncated Ligase 2 and 11.3 $\mu$ L of murine RNase inhibitor was  
651 then added to the sample. Samples were then incubated at 25°C for 1 hour. The  
652 samples were then purified using RNAClean XP beads according to the manufacturer's  
653 protocol.

## 654 **5. Second cDNA synthesis**

655 Purified samples were mixed with 1 $\mu$ L cDNA primer (IDT), 1 $\mu$ L dNTP mix up to a total  
656 volume of 12 $\mu$ L and incubated at 65°C for 5 min and then directly placed on ice. A  
657 1.5ml Eppendorf tube 8 $\mu$ L of the sample was mixed with 30 $\mu$ L of First Strand  
658 Buffer(5X), ), 7.5 $\mu$ L of DTT(0.1M), 7.5 $\mu$ L of DNase/RNase free water, 7.5 $\mu$ L of  
659 SuperScript<sup>®</sup> III Reverse transcriptase and 7.5 $\mu$ L of RNaseOUT<sup>TM</sup> Recombinant  
660 ribonuclease Inhibitor and incubated at 50°C for 1 hour followed by cDNA purification

661 using Agencourt RNAClean XP beads according to the manufacturer's protocol.  
 662 Samples were then stored at -20°C.

### 663 **6. PCR amplification**

664 Prior to PCR amplification, we determined that 20 cycles were required for appropriate  
 665 amplification. A total reaction volume of 25µL containing 2x KAPA mix, 0.04µM  
 666 PCRInPE2 (IDT), 0.4µM PCR InPE1.0 (IDT), 0.5µM PCR Index (IDT) and 5µL of  
 667 purified cDNA were amplified using the following protocol: 98°C for 3 min followed by  
 668 20 cycles at 98°C for 20 seconds, 60°C for 30 seconds , 72°C for 30 seconds followed  
 669 by 72°C for 5 minutes. The libraries were purified according to the manufacturer's  
 670 protocol and eluted in 20µL EB (elution buffer). The samples were then stored at -20°C  
 671 until used.

### 672 **7. Quality control of Libraries**

673 The average length of the prepared libraries was quantified using an Agilent DNA 1000  
 674 high sensitivity kit with a 2100 Bioanalyzer. The concentration of the libraries was  
 675 determined using a Qubit dsDNA HS kit. The libraries were diluted to 4nM, pooled and  
 676 denatured before sequencing on the Illumina NextSeq platform using paired-end  
 677 sequencing. We used 30 cycles for read 1 and 270 cycles for read 2 during  
 678 sequencing.

#### *Sequence*

<i>Ligation Adapter</i>	/5rApp/AGATCGGAAGAGCACACGTCTGAACTCCAGTCAC/3d- dC/
<i>cDNA primer</i>	GTGACTGGAGTTCAGACGTGTGCTCTTCCGA
<i>PCR primer INPE1</i>	AATGATACGGCGACCACCGAGATCTACACTCTTTCCCTACACGACGCTCTT- CCGATCT
<i>PCR primer INPE2</i>	GTGACTGGAGTTCAGACGTGTGCTCTTCCGATCT
<i>PCR index primer</i>	CAAGCAGAAGACGGCATAACGAGATCGTGATGTGACTGGAGTTC

679

680



681

682

### 683 **Postprocessing Spatial Transcriptomics**

684 First, we aligned the H&E staining by the use of the st-pipeline  
685 ([github.com/SpatialTranscriptomics-Research/st\\_pipeline](https://github.com/SpatialTranscriptomics-Research/st_pipeline)). The pipeline contains the  
686 following steps: Quality trimming and removing of low quality bases (bases with quality  
687 < 10), sanity check (reads same length, reads order, etc.), remove homopolymers,  
688 normalize for AT and GC content, mapping the read2 with STAR, demultiplexing based  
689 on read1, sort for reads (read1) with valid barcodes, annotate the reads with htseq-  
690 count, group annotated reads by barcode (spot position), gene and genomic location  
691 (with an offset) to get a read count ([github.com/SpatialTranscriptomics-  
692 Research/st\\_pipeline](https://github.com/SpatialTranscriptomics-Research/st_pipeline)). The pipeline resulted in a gene count matrix and a spatial  
693 information file containing the x and y position and the H&E image. We used the Seurat  
694 v3.0 package to normalize gene expression values by dividing each estimated cell by  
695 the total number of transcripts and multiplied by 10,000, followed by natural-log  
696 transformation. As described for sc-RNA sequencing, we removed batch effects and  
697 scaled data by a regression model including sample batch and percentage of  
698 ribosomal and mitochondrial gene expression. For further analysis we used the 2000  
699 most variable expressed genes and decomposed eigenvalue frequencies of the first  
700 100 principal components and determined the number of non-trivial components by  
701 comparison to randomized expression values. The obtained non-trivial components  
702 were used for SNN clustering followed by dimensional reduction using the UMAP  
703 algorithm. Differently expressed genes (DE) of each cluster were obtained using a  
704 hurdle model tailored to scRNA-seq data which is part of the MAST package. We  
705 further build a user-friendly viewer for spatial transcriptomic data and provide tutorials  
706 on analysis of data: <https://themilolab.github.io/SPATA/index.html>.

707

### 708 **Spatial gene expression**

709 For spatial expression plots, we used either normalized and scaled gene expression  
710 values (to plot single genes) or scores of a set of genes, using the 0.5 quantile of a  
711 probability distribution fitting. The x-axis and y-axis coordinates are given by the input  
712 file based on the localization at the H&E staining. We computed a matrix based on the  
713 maximum and minimum extension of the spots used (32x33) containing the gene  
714 expression or computed scores. Spots without tissue covering were set to zero. Next,

715 we transformed the matrix, using the squared distance between two points divided by  
 716 a given threshold, implemented in the fields package (R-software) and adapted the  
 717 input values by increasing the contrast between uncovered spots. The data are  
 718 illustrated either as surface plots (plotly package R-software) or as images (graphics  
 719 package R-software).

720

## 721 **Representation of Cellular States**

722 We aligned cells/spots to variable states with regard to gene sets (GS) that were  
 723 selected  $GS_{(1,2,..n)}$ . First, we separated cells into  $GS_{(1+2)}$  versus  $GS_{(2+4)}$ , using the  
 724 following equation:

$$725 \quad A_1 = \|GS_{(1)}, GS_{(2)}\|_{\infty} - \|GS_{(3)}, GS_{(4)}\|_{\infty}$$

726  $A_1$  defines the y-axis of the two-dimensional representation. In a next step, we  
 727 calculated the x-axis separately for spots  $A_1 < 0$  and  $A_1 > 0$ :

$$728 \quad A_1 > 0: A_2 = \log_2 (\overline{GS_{(1)}} - [\overline{GS_{(2)}} + 1])$$

$$729 \quad A_1 < 0: A_2 = \log_2 (\overline{GS_{(3)}} - [\overline{GS_{(4)}}])$$

730 For further visualization of the enrichment of subsets of cells according to gene set  
 731 enrichment across the two-dimensional representation, we transformed the distribution  
 732 to representative colors using a probability distribution fitting. This representation is an  
 733 adapted method published by Neftel and colleagues recently<sup>20,28</sup>.

734

## 735 **Spatial correlation analysis**

736 The spatial correlation was performed by integrating a deep autoencoder for  
 737 background noise reduction and a Bayesian correlation model. In a first step, we  
 738 performed noise reduction through an autoencoder similar to recent described for  
 739 single-cell RNA-sequencing studies<sup>39</sup>. The autoencoder consist of an encoder and  
 740 decoder part which can be defined as transitions:

$$741 \quad (1) \text{ encoder: } \phi: \mathcal{X} \rightarrow \mathcal{F} \text{ decoder: } \psi: \mathcal{F} \rightarrow \mathcal{X}$$

$$742 \quad (2) \phi, \psi = \arg.\min \|X - (\phi, \psi)X\|^2$$

743 The encoder stage of an autoencoder takes the input  $x \in \mathbb{R}^d = \mathcal{X}$  and maps it to  $z \in$   
 744  $\mathbb{R}^p = \mathcal{F}$  at the layer position  $\varphi$  :

$$745 \quad (3) x = A^{\varphi=0} ; z^{\varphi} = \mathbf{ReLU}(W^{\varphi} \times A^{\varphi-1} + b^{\varphi})$$

746  $z^{\varphi}$  is also referred to as *latent representation*, here presented as  $z^1, z^2, \dots, z^{\varphi=n}$  in  
 747 which  $\varphi$  describes the number of hidden layers.  $\mathbf{W}$  is the weight matrix and  $\mathbf{b}$  represent  
 748 the dropout or bias vector. Our network architecture contained 32 hidden layers, as

749 recommended<sup>39</sup>. In the decoder weights and biases are reconstructed through  
750 backpropagation ( $\psi: \mathcal{F} \rightarrow \mathcal{X}$ ) and  $z$  is mapped to  $x' = A^{0'}$  in the shape as  $x'$ .

$$751 \quad (4) \quad A^{\varphi-1'} = \sigma'(W^{\varphi'} \times z^{\varphi} + b^{\varphi'})$$

752 In this context,  $W', \sigma', b'$  from the decoder are unrelated to  $W, \sigma, b$  from the encoder.  
753 We used a loss function to train the network in order to minimize reconstruction errors.

$$754 \quad (5) \quad \mathcal{L}(x, x') = \|x - \sigma'(W'(\sigma(Wx + b)) + b')\|^2$$

755 In the second step, we used the predicted gene expression matrix ( $x'$ ) and fitted and  
756 Bayesian correlation model (Bayesian First Aid,  
757 [https://github.com/rasmusab/bayesian\\_first\\_aid](https://github.com/rasmusab/bayesian_first_aid)). An illustration of the spatial  
758 correlation is given in the **supplementary figure 7**

759

## 760 **sc-RNA-sequencing integration into spatial context**

761 In order to integrate determined cluster into the spatial context of the spatial  
762 transcriptomic data. We used the recent published spotlighted algorithm and integrated  
763 the output into our SPATA objects for visualization<sup>21</sup>.

764

## 765 **RNA-velocity and Pseudotime trajectory analysis**

766 In order to determine dynamic gene expression changes, we extracted spliced and  
767 unspliced genes from the bam output created by cell ranger using the velocity.py tool<sup>40</sup>  
768 . The resulting \*.loom files were merged and transformed into .h5ad format for further  
769 processing by scVelo<sup>41</sup> and CellRank<sup>42</sup>. The pipeline is integrated into the SPATA  
770 toolbox<sup>43</sup>. Single-cell data are reformatted into an SPATA S4 object using the UMAP  
771 coordinates as spatial coordinates. Outputs of the scVelo script (implemented in the  
772 development branch of the SPATA toolbox) are imported into the SPATA S4 object  
773 (*slot:@fdata*) and available for visualization. RNA-velocity streams are converted into  
774 trajectories and imported to the SPATA S4 object (*slot:@trajectories*). Dynamic gene  
775 expression changes along trajectories are performed by the `assessTrajectoryTrends()`  
776 function.

777

## 778 **Gene set enrichment analysis**

779 Gene sets were obtained from the database MSigDB v7 and internally created gene  
780 sets are available at [github.com/heilandd](https://github.com/heilandd). For enrichment analysis of single clusters,  
781 the normalized and centered expression data were used and further transformed to z-

782 scores ranging from 1 to 0. Genes were ranked in accordance to the obtained  
783 differential expression values and used as the input for GSEA.

784

785

### 786 **Identification of cycling cells**

787 We used the set of genes published by Neftel and colleagues to calculate proliferation  
788 scores based on the GSVA package implemented in R-software. The analysis based  
789 on a non-parametric unsupervised approach, which transformed a classic gene matrix  
790 (gene-by-sample) into a gene set by sample matrix resulted in an enrichment score for  
791 each sample and pathway. From the output enrichment scores we set a threshold  
792 based on distribution fitting to define cycling cells.

793

### 794 **Nearest Functionally Connected Neighbor (NFCN)**

795 To identify connected cells that interact by defined activation or inhibition of down-  
796 stream signals in the responder cell, we created a novel model. Therefore, we  
797 assumed that a cell-cell interaction is given only if a receptor/ligand pair induce  
798 correspondent down-stream signaling within the responder cell (cell with expressed  
799 receptor). Furthermore, we take into account that the importance of an activator cell  
800 (cell with expressed ligand) can be ranked according to their enriched signaling, which  
801 is responsible for inducing ligand expression. Based on these assumptions we defined  
802 an algorithm to map cells along an interaction-trajectory. The algorithm was designed  
803 to identify potential activators from a defined subset of cells.

804 As input for the analysis we used a normalized and scaled gene expression matrix, a  
805 string containing the subset of target cells, a list of genes defining ligand induction on  
806 the one side and receptor signaling on the other side. These genes were chosen either  
807 by the MSigDB v7 database or our stimulation library explained above. Next, we down-  
808 scaled the data to 3000 representative cells including all myeloid cell types and  
809 calculated the enrichment of induction and activation of the receptor/ligand pair.  
810 Enrichment scores were calculated by singular value decomposition (SVD) over the  
811 genes in the gene set and the coefficients of the first right-singular vector defined the  
812 enrichment of induction/activation profile. Both expression values and enrichment  
813 scores were fitted by a probability distribution model and cells outside the 95% quantile  
814 were removed. Next, we fitted a model using a non-parametric kernel estimation  
815 (Gaussian or Cauchy-Kernel), on the basis of receptor/ligand expression ( $A_{exp}$ ) and

816 up/downstream signaling ( $A_{\text{eff}}$ ) of each cell ( $i=\{1,..n\}$ ). Both input vectors were  
817 normalized and z-scored:

818

$$819 \quad (1) n_{\text{exp } i} = \frac{A_{\text{exp } i} - \min(A_{\text{exp}})}{\max(A_{\text{exp}}) - \min(A_{\text{exp}})} \quad (2) \hat{f}_h(n_{\text{exp } i}) = \frac{1}{n} \sum_{i=1}^n K_h(n_{\text{exp}} - n_{\text{exp } i})$$

820

821 K is the kernel and  $0.7 > h > 0.3$  is used to adjust the estimator. The model resulted in  
822 a trajectory which was defined as Ligand<sup>(-)</sup>-Induction<sup>(-)</sup> to cells of the target subset with  
823 Receptor<sup>(-)</sup>-Activation<sup>(-)</sup>. Further cells were aligned along the “interaction-trajectory”. We  
824 defined connected cells by reaching the upper 70% CI in receptor/ligand expression  
825 as well as scores of induction/activation. The process of representation is illustrated  
826 schematically in **Supplementary Figure 4**. Additionally we determined receptor-ligand  
827 interaction by the NicheNet software as recommended by the authors<sup>44</sup>.

828

#### 829 **CNV estimation:**

830 Copy-number Variations (CNVs) were estimated by aligning genes to their  
831 chromosomal location and applying a moving average to the relative expression  
832 values, with a sliding window of 100 genes within each chromosome, as described  
833 recently<sup>18</sup>. First, we arranged genes in accordance to their respective genomic  
834 localization using the CONICSmatrix package (R-software). As a reference set of non-  
835 malignant cells, we in-silico extracted 400 CD8 positive cells (unlikely to be expressed  
836 on tumor cells). To avoid the considerable impact of any particular gene on the moving  
837 average we limited the relative expression values  $[-2.6, 2.6]$  by replacing all values  
838 above/below  $\text{exp}(\theta)=|2.6|$ , by using the infercnv package (R-software). This was  
839 performed only in the context of CNV estimation as previous reported<sup>11</sup>.

840

#### 841 **Flow cytometry:**

842 Single-Cell suspensions were obtained after Dead-Cell Removal and CD3 MACS-  
843 enrichment. Cells were incubated with VivaFix™ 398/550 (BioRad Laboratories, CA,  
844 USA) according to the manufacturer’s instructions. Cells were fixed in 4%  
845 paraformaldehyde (PFA) for 10 minutes. After centrifugation (350 g; 4°C; 5 min) and  
846 removal of the supernatant, the cell pellet was suspended in 0.5 ml 4°C cold FACS  
847 buffer. Cell suspensions were washed and centrifuged at 350xg for 5 mins, followed  
848 by resuspension in FACS buffer. The washing step was repeated twice. Finally, cells  
849 were resuspended in at least 0.5 to 1 mL of FACS buffer depending on the number of

850 cells. We used a Sony SP6800 spectral analyzer in standardization mode with PMT  
851 voltage set to maximum to reach a saturation rate below 0.1 %. Gating was performed  
852 by FCS Express 7 plus at the Lighthouse Core Facility, University of Freiburg.

853

### 854 **Immunofluorescence**

855 The same protocol was followed for human neocortical slices with or without microglia  
856 and tumor cell injection. The media was removed and exchanged for 1 mL of 4%  
857 paraformaldehyde (PFA) for 1 h and further incubated in 20% methanol in PBS for 5  
858 minutes. Slices were then permeabilized by incubating in PBS supplemented with 1 %  
859 Triton (TX-100) overnight at 4°C and further blocked using 20% BSA for 4 hours. The  
860 permeabilized and blocked slices were then incubated by primary antibodies in 5%  
861 BSA-PBS incubated overnight at 4°C. After washing in PBS, slices were labelled with  
862 secondary antibodies conjugated with Alexa 405, 488, 555, or 568 for 3 hours at room  
863 temperature. Finally, slices were mounted on glass slides using DAPI fluoromount  
864 (Southern Biotech, Cat. No. 0100-20), as recently described<sup>15</sup>.

865

### 866 **Human Organotypic Slice Culture**

867 Human neocortical slices were prepared as recently described<sup>15,25</sup>. Capillaries and  
868 damaged tissue were dissected away from the tissue block in the preparation medium  
869 containing Hibernate medium supplemented with 13 mM D+ Glucose and 30 mM  
870 NMDG. Coronal slices of 300 µm thickness were sectioned using a vibratome  
871 (VT1200, Leica Germany) and incubated in preparation medium for 10 minutes before  
872 plating to avoid any variability due to tissue trauma. Three to four slices were gathered  
873 per insert. The transfer of the slices was facilitated by a polished wide mouth glass  
874 pipette. Slices were maintained in growth medium containing Neurobasal (L-  
875 Glutamine) supplemented with 2% serum free B-27, 2% Anti- Anti, 10 mM D+ Glucose,  
876 1 mM MgSO<sub>4</sub>, and 1 mM Glutamax at 5% CO<sub>2</sub> and 37 °C. The entire medium was  
877 replaced with fresh culture medium 24 hours post plating, and every 48 hours  
878 thereafter.

879

880

881

882

883

884 **Chemical depletion of Microglia from slice cultures**

885 Selective depletion of the myeloid cell compartment in human neocortical slices was  
886 performed by supplementing the growth medium with 50  $\mu$ M for 24hrs and 11  $\mu$ M of  
887 Clodronate (Sigma, D4434) for the next 48hrs at 37°C. Subsequently, the slices were  
888 carefully rinsed with growth medium to wash away any debris.

889

890 **Tumor/T cell injection onto tissue cultures**

891 *ZsGreen* tagged BTSC#233 cell lines cultured and prepared as described in the cell  
892 culture section. Post trypsinization, a centrifugation step was performed, following  
893 which the cells were harvested and suspended in MEM media at 20,000 cells/ $\mu$ l. A 10  
894  $\mu$ L Hamilton syringe was used to inject 1  $\mu$ L of GBM cells into the slices and were  
895 incubated at 37°C for 3 days with a medium change every other days.

896 Blood samples were collected from the same donors from whom we obtained the  
897 healthy cortex for our organotypic slice cultures. Peripheral T cells were isolated using  
898 the same MACSxpress® Whole Blood Pan T Cell Isolation Kit (Miltenyi Biotech) and  
899 erythrocytes were eliminated from the suspension using ACK-lysis buffer (Thermo  
900 Fisher Scientific). T cells were tagged using the Cell Trace Far Red dye (Thermo Fisher  
901 Scientific) prior to injection into the slices. To block endogenous IL-10 receptor in T-  
902 cells, the neutralizing antibody anti-IL10 hAB (R&D systems) were added to the cells  
903 at the concentration of 5  $\mu$ g/ml for 1h and incubated at 37°C . Both IL10 knock out T  
904 cells and normal T cells were injected onto the sections and left it for another 48hrs at  
905 37°C.

906

907 **Enzyme linked Immunosorbent Assay**

908 An enzyme linked immunosorbent assay (ELISA) was performed in order to measure  
909 cytokine concentrations of IL-2, IL-10, IL-13 and IFN-gamma in the cell culture medium  
910 48h after T cell injection. The Multi-Analyte ELISArray Kit (Qiagen, Venlo, Netherlands;  
911 MEH-003A) was used according to the manufacturer's instructions. Absorbance was  
912 measured using the Tecan Infinite® 200 (Tecan, Männedorf, Switzerland).

913

914 **Treatment of patient with JAK-inhibitor**

915 A patient with a recurrent glioblastoma was treated with a daily dose of 40mg  
916 Ruxolitinib for 4 weeks. Before treatment, we confirmed the progress by a biopsy. The

917 treatment was performed as a neoadjuvant therapy. After 4 weeks, the patient  
918 underwent a gross-total surgery and adjuvant Temozolomide therapy.

919

920

### 921 **Acknowledgement**

922 DHH is funded by the Else-Kröner Stiftung and BMBF. VM Ravi was partially funded  
923 by the BMBF-projects FMT (13GW0230A). We thank Manching Ku and Dietmar Pfeifer  
924 for their helpful advice. We acknowledge Biorender.com.

925

### 926 **Conflict of interests**

927 No potential conflicts of interest were disclosed by the authors.

928

929

### 930 **Data availability**

931 scRNA-Sequencing Data available: (in preparation), Accession codes:  
932 [www.github.com/heilandd/VisLabv1.5](https://github.com/heilandd/VisLabv1.5) [https://github.com/heilandd/Vis\\_Lab1.5](https://github.com/heilandd/Vis_Lab1.5), NFCN  
933 Algorithm [www.github.com/heilandd/NFCN](https://github.com/heilandd/NFCN), SPATA-Lab: [www.github.com/heilandd/](https://github.com/heilandd/SPATA-Lab)  
934 [SPATA-Lab](https://github.com/heilandd/SPATA-Lab). Further information and requests for resources, raw data and reagents  
935 should be directed and will be fulfilled by the Contact: D. H. Heiland,  
936 [dieter.henrik.heiland@uniklinik-freiburg.de](mailto:dieter.henrik.heiland@uniklinik-freiburg.de).

937

938



939

940 Bibliography

941

- 942 1. Darmanis, S. *et al.* Single-Cell RNA-Seq Analysis of Infiltrating Neoplastic Cells at  
943 the Migrating Front of Human Glioblastoma. *Cell Rep.* **21**, 1399–1410 (2017).
- 944 2. Woroniecka, K. *et al.* T-Cell Exhaustion Signatures Vary with Tumor Type and Are  
945 Severe in Glioblastoma. *Clin. Cancer Res.* **24**, 4175–4186 (2018).
- 946 3. Chen, Z. & Hambardzumyan, D. Immune microenvironment in glioblastoma  
947 subtypes. *Front. Immunol.* **9**, 1004 (2018).
- 948 4. Sankowski, R. *et al.* Mapping microglia states in the human brain through the  
949 integration of high-dimensional techniques. *Nat. Neurosci.* **22**, 2098–2110 (2019).
- 950 5. Zhang, L. *et al.* Lineage tracking reveals dynamic relationships of T cells in  
951 colorectal cancer. *Nature* **564**, 268–272 (2018).
- 952 6. Zheng, C. *et al.* Landscape of Infiltrating T Cells in Liver Cancer Revealed by  
953 Single-Cell Sequencing. *Cell* **169**, 1342–1356.e16 (2017).
- 954 7. Baitsch, L. *et al.* Exhaustion of tumor-specific CD8<sup>+</sup> T cells in metastases from  
955 melanoma patients. *J. Clin. Invest.* **121**, 2350–2360 (2011).
- 956 8. Singer, M. *et al.* A Distinct Gene Module for Dysfunction Uncoupled from Activation  
957 in Tumor-Infiltrating T Cells. *Cell* **166**, 1500–1511.e9 (2016).
- 958 9. Anderson, A. C., Joller, N. & Kuchroo, V. K. Lag-3, Tim-3, and TIGIT: Co-inhibitory  
959 Receptors with Specialized Functions in Immune Regulation. *Immunity* **44**, 989–  
960 1004 (2016).
- 961 10. Im, S. J. *et al.* Defining CD8<sup>+</sup> T cells that provide the proliferative burst after PD-1  
962 therapy. *Nature* **537**, 417–421 (2016).
- 963 11. Tirosh, I. *et al.* Dissecting the multicellular ecosystem of metastatic melanoma by  
964 single-cell RNA-seq. *Science* **352**, 189–196 (2016).
- 965 12. Platten, M., Ochs, K., Lemke, D., Opitz, C. & Wick, W. Microenvironmental clues  
966 for glioma immunotherapy. *Curr Neurol Neurosci Rep* **14**, 440 (2014).
- 967 13. Filley, A. C., Henriquez, M. & Dey, M. Recurrent glioma clinical trial, CheckMate-  
968 143: the game is not over yet. *Oncotarget* **8**, 91779–91794 (2017).
- 969 14. Weller, M. *et al.* Rindopepimut with temozolomide for patients with newly  
970 diagnosed, EGFRvIII-expressing glioblastoma (ACT IV): a randomised, double-  
971 blind, international phase 3 trial. *Lancet Oncol.* **18**, 1373–1385 (2017).
- 972 15. Henrik Heiland, D. *et al.* Tumor-associated reactive astrocytes aid the evolution of

- 973 immunosuppressive environment in glioblastoma. *Nat. Commun.* **10**, 2541 (2019).
- 974 16. Zhang, Z. *et al.* SCINA: A Semi-Supervised Subtyping Algorithm of Single Cells  
975 and Bulk Samples. *Genes (Basel)* **10**, (2019).
- 976 17. Aran, D. *et al.* Reference-based analysis of lung single-cell sequencing reveals a  
977 transitional profibrotic macrophage. *Nat. Immunol.* **20**, 163–172 (2019).
- 978 18. Patel, A. P. *et al.* Single-cell RNA-seq highlights intratumoral heterogeneity in  
979 primary glioblastoma. *Science* **344**, 1396–1401 (2014).
- 980 19. Chen, H. *et al.* Single-cell trajectories reconstruction, exploration and mapping of  
981 omics data with STREAM. *Nat. Commun.* **10**, 1903 (2019).
- 982 20. Neftel, C. *et al.* An integrative model of cellular states, plasticity, and genetics for  
983 glioblastoma. *Cell* **178**, 835–849.e21 (2019).
- 984 21. Elosua, M., Nieto, P., Mereu, E., Gut, I. & Heyn, H. SPOTlight: Seeded NMF  
985 regression to Deconvolute Spatial Transcriptomics Spots with Single-Cell  
986 Transcriptomes. *BioRxiv* (2020). doi:10.1101/2020.06.03.131334
- 987 22. Naito, Y., Takagi, T. & Higashimura, Y. Heme oxygenase-1 and anti-inflammatory  
988 M2 macrophages. *Arch. Biochem. Biophys.* **564**, 83–88 (2014).
- 989 23. Qin, Y. *et al.* A Milieu Molecule for TGF- $\beta$  Required for Microglia Function in the  
990 Nervous System. *Cell* **174**, 156–171.e16 (2018).
- 991 24. Giladi, A. *et al.* Dissecting cellular crosstalk by sequencing physically interacting  
992 cells. *Nat. Biotechnol.* **38**, 629–637 (2020).
- 993 25. Ravi, V. M. *et al.* Human organotypic brain slice culture: a novel framework for  
994 environmental research in neuro-oncology. *Life Sci. Alliance* **2**, (2019).
- 995 26. Kling, T. *et al.* Integrative Modeling Reveals Annexin A2-mediated Epigenetic  
996 Control of Mesenchymal Glioblastoma. *EBioMedicine* **12**, 72–85 (2016).
- 997 27. Venteicher, A. S. *et al.* Decoupling genetics, lineages, and microenvironment in  
998 IDH-mutant gliomas by single-cell RNA-seq. *Science* **355**, (2017).
- 999 28. Tirosh, I. *et al.* Single-cell RNA-seq supports a developmental hierarchy in human  
1000 oligodendroglioma. *Nature* **539**, 309–313 (2016).
- 1001 29. Blank, C. U. *et al.* Defining “T cell exhaustion”. *Nat. Rev. Immunol.* **19**, 665–674  
1002 (2019).
- 1003 30. Jiang, Y., Li, Y. & Zhu, B. T-cell exhaustion in the tumor microenvironment. *Cell*  
1004 *Death Dis.* **6**, e1792 (2015).
- 1005 31. Wherry, E. J. T cell exhaustion. *Nat. Immunol.* **12**, 492–499 (2011).
- 1006 32. Li, H. *et al.* Dysfunctional CD8 T Cells Form a Proliferative, Dynamically Regulated

1007           Compartment within Human Melanoma. *Cell* **176**, 775–789.e18 (2019).

1008 33. Woroniecka, K. I., Rhodin, K. E., Chongsathidkiet, P., Keith, K. A. & Fecci, P. E.  
1009           T-cell Dysfunction in Glioblastoma: Applying a New Framework. *Clin. Cancer Res.*  
1010           **24**, 3792–3802 (2018).

1011 34. Winkler, F. & Bengsch, B. Use of mass cytometry to profile human T cell  
1012           exhaustion. *Front. Immunol.* **10**, 3039 (2019).

1013 35. Wurm, J. *et al.* Astrogliosis Releases Pro-Oncogenic Chitinase 3-Like 1 Causing  
1014           MAPK Signaling in Glioblastoma. *Cancers (Basel)* (2019).

1015 36. Priego, N. *et al.* STAT3 labels a subpopulation of reactive astrocytes required for  
1016           brain metastasis. *Nat. Med.* **24**, 1024–1035 (2018).

1017 37. Kaiser, S. *et al.* Neuroprotection after Hemorrhagic Stroke Depends on Cerebral  
1018           Heme Oxygenase-1. *Antioxidants (Basel)* **8**, (2019).

1019 38. Sebastián, V. P. *et al.* Heme Oxygenase-1 as a Modulator of Intestinal  
1020           Inflammation Development and Progression. *Front. Immunol.* **9**, 1956 (2018).

1021 39. Eraslan, G., Simon, L. M., Mircea, M., Mueller, N. S. & Theis, F. J. Single-cell RNA-  
1022           seq denoising using a deep count autoencoder. *Nat. Commun.* **10**, 390 (2019).

1023 40. La Manno, G. *et al.* RNA velocity of single cells. *Nature* **560**, 494–498 (2018).

1024 41. Bergen, V., Lange, M., Peidli, S., Wolf, F. A. & Theis, F. J. Generalizing RNA  
1025           velocity to transient cell states through dynamical modeling. *Nat. Biotechnol.* **38**,  
1026           1408–1414 (2020).

1027 42. Lange, M. *et al.* CellRank for directed single-cell fate mapping. *BioRxiv* (2020).  
1028           doi:10.1101/2020.10.19.345983

1029 43. Kueckelhaus, J. *et al.* Inferring spatially transient gene expression pattern from  
1030           spatial transcriptomic studies. *BioRxiv* (2020). doi:10.1101/2020.10.20.346544

1031 44. Browaeys, R., Saelens, W. & Saeys, Y. NicheNet: modeling intercellular  
1032           communication by linking ligands to target genes. *Nat. Methods* **17**, 159–162  
1033           (2020).

1034

1035

1036

1037

1038

1039

1040

1041 **Figures:**

1042 **Figure 1: a)** Illustration of the workflow, tissue specimens were obtained from 11 glioblastoma patients.  
1043 Samples from 8 patients were used for scRNA-seq and 3 for spatial transcriptomics. **b)** Dimensional  
1044 reduction using UMAP, cell type was determined by SingleR ([github.com/dviraran/SingleR](https://github.com/dviraran/SingleR)). **c)**  
1045 Dimensional reduction (UMAP) of CD3+/CD8+ cells. SNN-clustering reveal 13 different clusters. RNA-  
1046 velocity based pseudotime is presented by streams obtained from dynamic modeling in scvelo. Marker  
1047 expression in different subpopulations ranked by grade of activity. **d)** Dimensional reduction plots of  
1048 estimated gene-set enrichment (left), of cell proliferation (middle) and regulatory marker genes (right).  
1049 **e,f)** Detailed presentation of 3 major trajectories and its changes of estimated pseudotime across  
1050 different models. Velocity trajectory 2 reveals almost no temporal changes, but is marked by increasing  
1051 IFNg signaling along the trajectory. **g)** Line plot of IFNg signalling gene expression along the velocity  
1052 trajectory 2 (left) and dimensional reduction (right). **h)** Inferring dynamic alterations along the trajectory  
1053 revealed up-regulation of IL-10 and TGF- $\beta$  signaling, presented as a line plot (top). **(i)** Gene set  
1054 enrichment analysis of the IL10 signaling enrichment in defined start and destination region of the  
1055 trajectory (bottom). **j)** Mapping of gene expression along the pseudotime trajectory. Bars at the bottom  
1056 indicate the enrichment of each cell to enrich effector or exhausted signatures. Line plots on the top,  
1057 showed enrichment for the T cell state signatures<sup>8</sup>.

1058

1059 **Figure 2: a)** Workflow of spatial transcriptomics **b)** 2D representation of heterogeneous states in  
1060 glioblastoma by Neftel, colors indicate the expression of cycling cells (quantile). **c)** H&E staining and **(d)**  
1061 gene expression enrichment maps of the mesenchymal state defined by Neftel<sup>20</sup>. **e)** Enrichment maps  
1062 of T cell clusters by spotlight algorithm<sup>21</sup> in different samples. Maps are colored by a normalized spotlight  
1063 score. **f)** Correlation heatmap of a Bayesian correlation model of T cell clusters and glioblastoma  
1064 transcriptional subtypes. **(g)** Scatter plots of spot-wise correlation of HAVCR2 and LAG3 expression  
1065 and T cells (left side), mesenchymal-like gene expression (middle) and NPC-like gene expression (right  
1066 side), Rho correlation and CI95% are given at the top.

1067

1068 **Figure 3: a)** Workflow exploring cell-cell interactions using two approaches: 1. Predict functional  
1069 neighbors based on defined ligand-receptor interaction. 2. Validation in spatial transcriptomic datasets.  
1070 **b)** Cell-cell interaction plot as explained in supplementary figure 4. Cells with an interaction-score above  
1071 0.95 are mapped to the UMAP. **c)** Volcano plot of differential gene expression between highly connected  
1072 cells (CI>97.5%, left side) vs non-connected cells (CI<2.5%, right side), adjusted  $-\log(p\text{-value})$  (FDR) was  
1073 used at the y-axis. Red cells are defined by fold-change above 2 and FDR < 0.05. **d)** Spatial surface  
1074 plots of gene expression and pathway enrichment. **e)** Multilayer representation of cellular interaction. At  
1075 the top layer, a UMAP is shown colored by expression levels of HMOX1. Each red line represents a cell  
1076 (upper CI>99% NFCNA-Score) and its most likely position within the spatial dataset. The second layer  
1077 is a spatial transcriptomic dataset, colored by the predicted NFCNA-score. At the bottom, the third layer  
1078 represents a UMAP colored accordingly to CD3 expression. Green lines showed the upper CI>99% of  
1079 receiver cells. **f)** Violin plots of the mean NFCNA score in each cluster. **g)** Violin plots of gene expression  
1080 between connected cells (CI>97.5%, left side) vs non-connected cells (CI<2.5%, right side). Wilcoxon  
1081 Rank Sum test and FDR adjustment was used for statistical testing. **h)** Gene Set enrichment analysis

1082 of four different gene sets. **i)** Heatmap of differently expressed genes or connected myeloid (right) and  
1083 lymphoid (middle) cells and the cluster of doublets. At the top, scatterplot of total UMIs per cell in each  
1084 group.

1085  
1086  
1087

1088 **Figure 4:** **a)** Experimental workflow of the neocortical GBM model autografted with patient derived T  
1089 cells and with/without myeloid cell depletion. **b)** Immunostainings of IBA1 (Macrophages and Microglia)  
1090 in magenta and HMOX1 in cyan, tumor cells are depicted in grey. In the upper panel, the control set  
1091 with no myeloid cell depletion ( $M^+$ ) is shown, the bottom panel contains the myeloid cell depleted  
1092 sections. **c)** ELISA measurements of IL10 **d)** Immunostainings of T cells (CSFE-Tagged, in red) and  
1093 GZMB, a marker of T cell activation (green). **e, f)** ELISA measurements of IL2 and IFN $\gamma$  **g)**  
1094 Immunostainings of TIM3 (gene: HAVCR2) in yellow, which was identified in the ScRNA-seq, and T cell  
1095 in red. **h)** Illustration of the workflow. **i)** Immunostainings of tumor cells (grey), T cells (CSFE-Tagged, in  
1096 red) and GZMB a marker of T cell activation (green) with pre-treatment in anti-IL-10R antibodies. **j)**  
1097 ELISA measurements of IL2 in ctr and IL10R inhibition. **k)** Immunostainings of tumor cells (grey), T cells  
1098 (CSFE-Tagged, in red) and GZMB a marker of T cell activation (green) treated with JAK-inhibitor  
1099 Ruxolitinib. **l)** Heatmap of interleukin intensities different environment. Information regarding the  
1100 presence of myeloid cells are given at the bottom. **m)** Illustration of the workflow of JAK inhibition in a  
1101 recurrent GBM patient. **n-o)** Immunohistochemistry of immune marker and its quantification, white: pre  
1102 therapy, gray: post therapy **p)** Dimensional reduction of single-cell RNA-sequencing of the Ruxolitinib  
1103 treated patient revealed a large percentage of T cells (right side). **q)** Comparison of T cells from the  
1104 Ruxolitinib treated patient and the non-treated cohort. **r)** A barplot that indicates the cluster specific  
1105 enrichment of JAK treated T cells. P-values are determined by one-way ANOVA (c,e,f,j) adjusted by  
1106 Benjamini- Hochberger (c,e,f,j) for multiple testing. Data is given as mean  $\pm$  standard deviation.

1107

## 1108 **Supplementary Figures:**

1109

1110 **Supplementary Figure 1:** a) Workflow and representative FACS images. b) UMAP representation of  
1111 all detected cell types. c) Distribution of patients across all clusters and cell types. d) UMAP  
1112 representation of all determined clusters (SNN) e) The graph representing the percentage of each  
1113 patient in different clusters f) Signature genes of each cluster g-i) UMAP representation of Isolated T  
1114 cells spitted into CD4+ and CD8+ cells and the total number of clusters (13). j) Heatmap of signature  
1115 genes

1116

1117 **Supplementary Figure 2:** a) Copy-number alterations based on single cell data. Only a small subset  
1118 of tumor cells was found in the OPC cluster. b) Gene expression maps of common marker genes.

1119

1120 **Supplementary Figure 3:** a) Workflow to build a library of stimulated T-cells b) T cell stimulation in  
1121 order to build a library for cytokine effects, illustrated is a heatmap of the 10 most significant marker  
1122 genes of each stimulation state, based on PAMR algorithm implemented in the AutoPipe. c) Dimensional

1123 reduction (UMAP) of gene expression of the different simulation experiments. d) Z-scored expression  
1124 of each stimulation signature along the velocity trajectory 1 (Figure 1).

1125

1126 **Supplementary Figure 4:** a) Workflow and concept of the NFCN Analysis

1127

1128 **Supplementary Figure 5:** a) Results from the Nichnet algorithm, left: The receptor-target interaction,  
1129 right: the receptor-ligand network.

1130

1131 **Supplementary Figure 6:** a) Kaplan-Meier survival estimation of HMOX1 high/low expression GBM. b-  
1132 c) Expression of HMOX1 in different regions of the tumor (b) and in de-novo and recurrent stage (c).

1133

1134 **Supplementary Figure 7:** a) Illustration of the workflow to determine the spatial correlation using a  
1135 deep autoencoder for denoising followed by a Bayesian correlation model. b) Examples of the predicted  
1136 overlap of T cells and CD163/HMOX1(+) myeloid cells. c) Distribution of the predicted correlation.

1137

# Figures

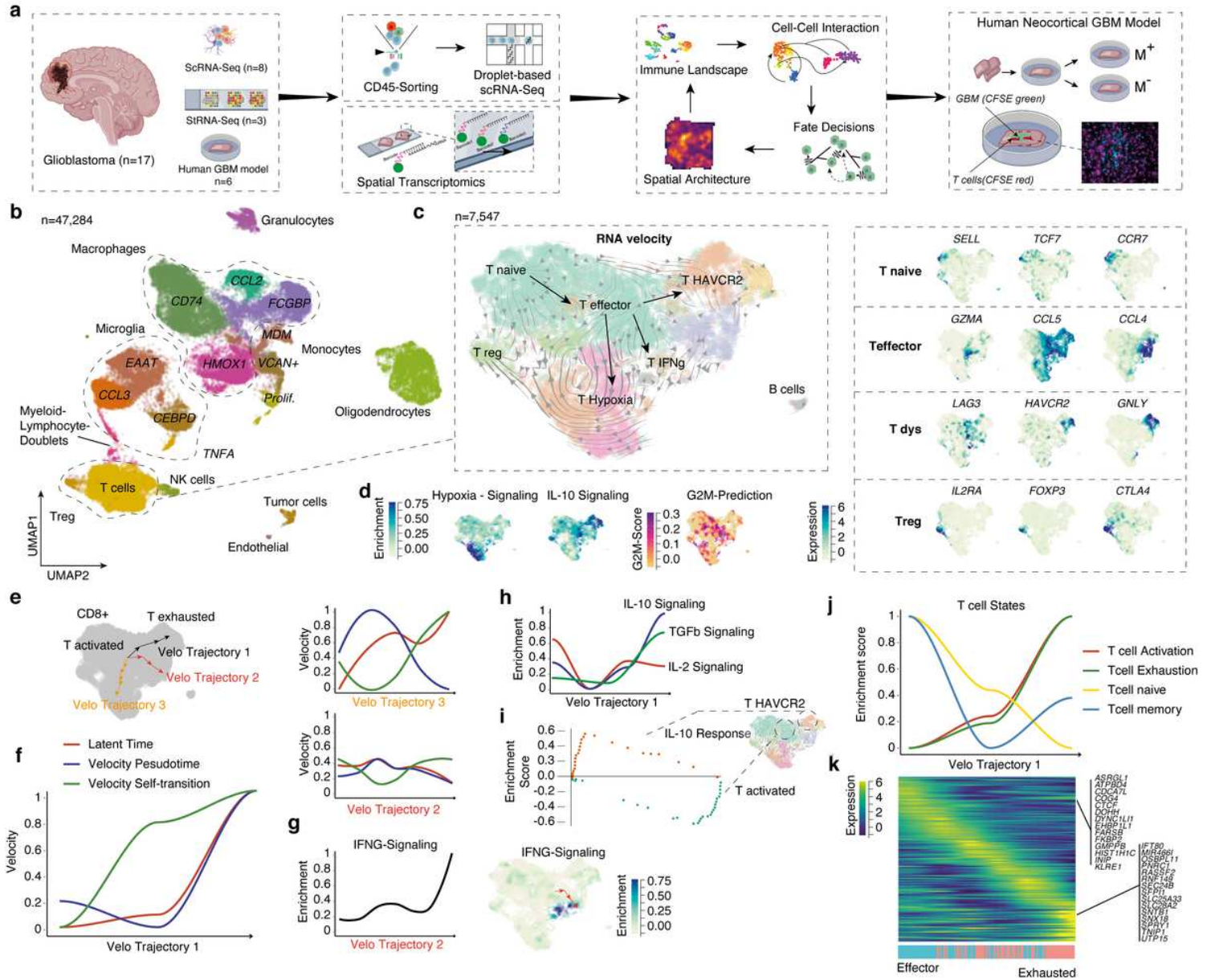


**Figure 1**

a) Illustration of the workflow, tissue specimens were obtained from 11 glioblastoma patients. Samples from 8 patients were used for scRNA-seq and 3 for spatial transcriptomics. b) Dimensional reduction using UMAP, cell type was determined by SingleR ([github.com/dviraran/SingleR](https://github.com/dviraran/SingleR)). c) Dimensional reduction (UMAP) of CD3<sup>+</sup>/CD8<sup>+</sup> cells. SNN-clustering reveal 13 different clusters. RNA-velocity based pseudotime is presented by streams obtained from dynamic modeling in scvelo. Marker expression in different subpopulations ranked by grade of activity. d) Dimensional reduction plots of estimated gene-set enrichment (left), of cell proliferation (middle) and regulatory marker genes (right). e,f) Detailed presentation of 3 major trajectories and its changes of estimated pseudotime across different models. Velocity trajectory 2 reveals almost no temporal changes, but is marked by increasing IFNg signaling



along the trajectory. g) Line plot of IFN $\gamma$  signalling gene expression along the velocity trajectory 2 (left) and dimensional reduction (right). h) Inferring dynamic alterations along the trajectory revealed up-regulation of IL-10 and TGF- $\beta$  signaling, presented as a line plot (top). (i) Gene set enrichment analysis of the IL10 signaling enrichment in defined start and destination region of the trajectory (bottom). j) Mapping of gene expression along the pseudotime trajectory. Bars at the bottom indicate the enrichment of each cell to enrich effector or exhausted signatures. Line plots on the top, showed enrichment for the T cell state signatures<sup>8</sup>.

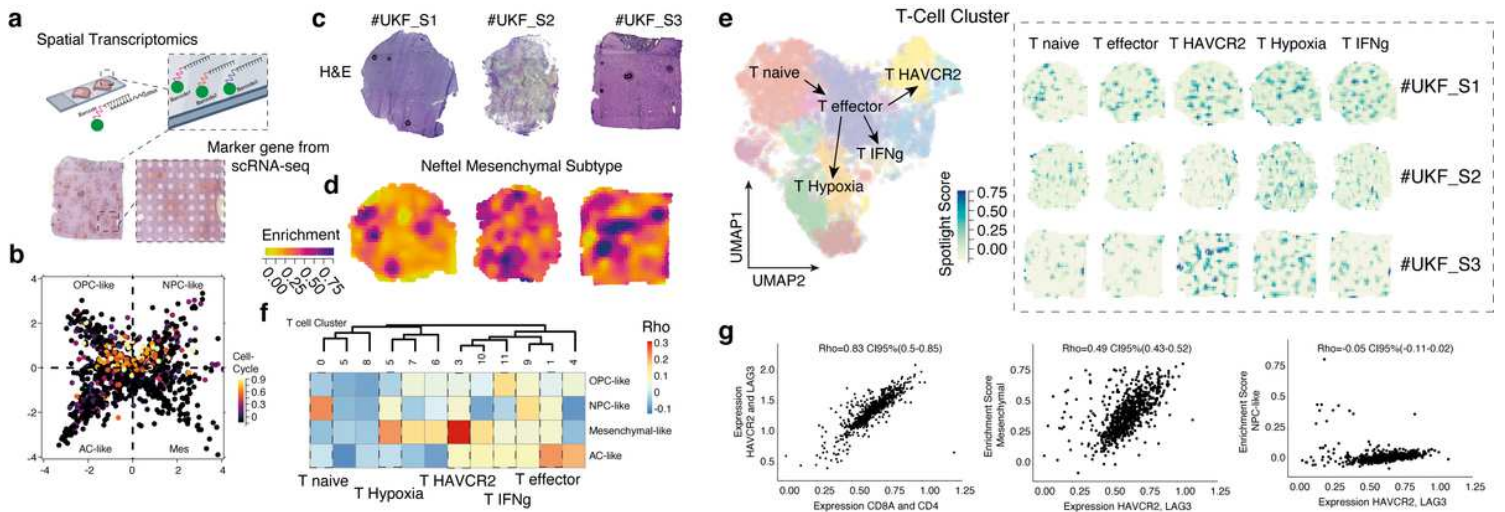


**Figure 2**

a) Workflow of spatial transcriptomics b) 2D representation of heterogeneous states in glioblastoma by Nefitel, colors indicate the expression of cycling cells (quantile). c) H&E staining and (d) gene expression enrichment maps of the mesenchymal state defined by Nefitel20. e) Enrichment maps of T cell clusters by spotlight algorithm<sup>21</sup> in different samples. Maps are colored by a normalized spotlight 1 score. f) Correlation heatmap of a Bayesian correlation model of T cell clusters and glioblastoma transcriptional subtypes. (g) Scatter plots of spot-wise correlation of HAVCR2 and LAG3 expression and T cells (left side), mesenchymal-like gene expression (middle) and NPC-like gene expression (right 1065 side), Rho correlation and CI95% are given at the top.



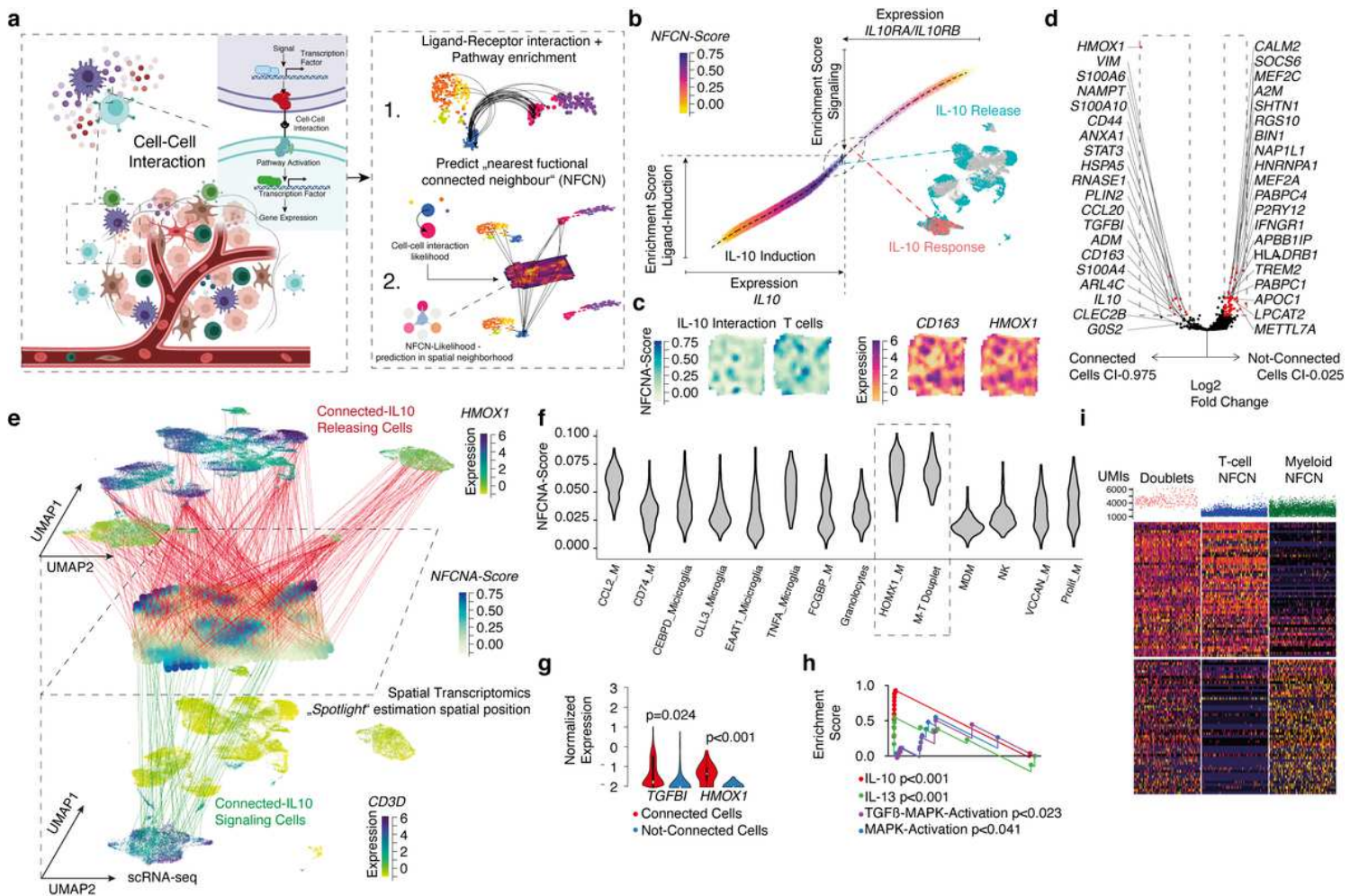


**Figure 3**

a) Workflow exploring cell-cell interactions using two approaches: 1. Predict functional neighbors based on defined ligand-receptor interaction. 2. Validation in spatial transcriptomic datasets. b) Cell-cell interaction plot as explained in supplementary figure 4. Cells with an interaction-score above 0.95 are mapped to the UMAP. c) Volcano plot of differential gene expression between highly connected cells (CI>97.5%, left side) vs non-connected cells (CI<2.5%, right side), adjusted  $-\log(p\text{-value})$  (FDR) was used at the y-axis. Red cells are defined by fold-change above 2 and FDR < 0.05. d) Spatial surface plots of gene expression and pathway enrichment. e) Multilayer representation of cellular interaction. At the top layer, a UMAP is shown colored by expression levels of HMOX1. Each red line represents a cell (upper CI>99% NFCNA-Score) and its most likely position within the spatial dataset. The second layer is a spatial transcriptomic dataset, colored by the predicted NFCNA-score. At the bottom, the third layer represents a UMAP colored accordingly to CD3 expression. Green lines showed the upper CI>99% of receiver cells. f) Violin plots of the mean NFCNA score in each cluster. g) Violin plots of gene expression between connected cells (CI>97.5%, left side) vs non-connected cells (CI<2.5%, right side). Wilcoxon Rank Sum test and FDR adjustment was used for statistical testing. h) Gene Set enrichment analysis of four different gene sets. i) Heatmap of differentially expressed genes or connected myeloid (right) and lymphoid (middle) cells and the cluster of doublets. At the top, scatterplot of total UMIs per cell in each 1083 group.

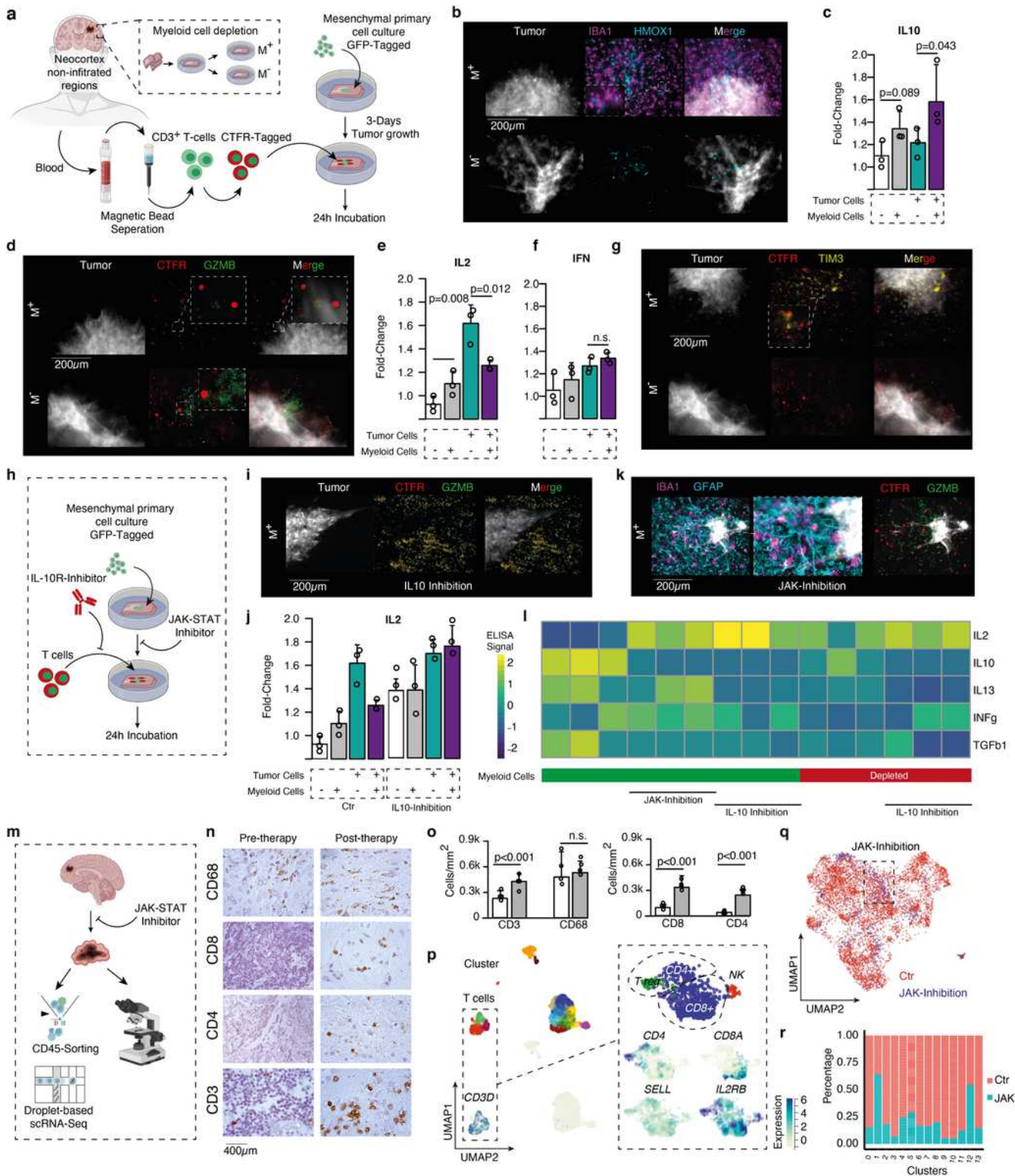


**Figure 4**

a) Experimental workflow of the neocortical GBM model autografted with patient derived T cells and with/without myeloid cell depletion. b) Immunostainings of IBA1 (Macrophages and Microglia) in magenta and HMOX1 in cyan, tumor cells are depicted in grey. In the upper panel, the control set with no myeloid cell depletion ( $M^+$ ) is shown, the bottom panel contains the myeloid cell depleted sections. c) ELISA measurements of IL10 d) Immunostainings of T cells (CSFE-Tagged, in red) and 1 GZMB, a marker

of T cell activation (green). ). e, f) ELISA measurements of IL2 and IFN $\gamma$  g) Immunostainings of TIM3 (gene: HAVCR2) in yellow, which was identified in the ScRNA-seq, and T cell in red. h) Illustration of the workflow. i) Immunostainings of tumor cells (grey), T cells (CSFE-Tagged, in red) and GZMB a marker of T cell activation (green) with pre-treatment in anti-IL-10R antibodies. j) ELISA measurements of IL2 in ctr and IL10R inhibition. k) Immunostainings of tumor cells (grey), T cells (CSFE-Tagged, in red) and GZMB a marker of T cell activation (green) treated with JAK-inhibitor Ruxolitinib. l) Heatmap of interleukin intensities different environment. Information regarding the presence of myeloid cells are given at the bottom. m) Illustration of the workflow of JAK inhibition in a recurrent GBM patient. n-o) Immunohistochemistry of immune marker and its quantification, white: pre therapy, gray: post therapy p) Dimensional reduction of single-cell RNA-sequencing of the Ruxolitinib treated patient revealed a large percentage of T cells (right side). q) Comparison of T cells from the Ruxolitinib treated patient and the non-treated cohort. r) A barplot that indicates the cluster specific enrichment of JAK treated T cells. P-values are determined by one-way ANOVA (c,e,f,j) adjusted by Benjamini- Hochberger (c,e,f,j) for multiple testing. Data is given as mean  $\pm$  standard deviation.

## Supplementary Files

This is a list of supplementary files associated with this preprint. Click to download.

- [Supplementary1.pdf](#)
- [Supplementary2.pdf](#)
- [Supplementary3.pdf](#)
- [Supplementary4.pdf](#)
- [Supplementary5.pdf](#)
- [Supplementary6.pdf](#)
- [Supplementary7.pdf](#)